Modelling of biodiesel fuel droplet heating and evaporation

Sazhin, S.S. , Al Qubeissi, M. , Kolodnytska, R. , Elwardany, A.E. , Nasiri, R. and Heikel, M.R.

Original citation:
Sazhin, S.S. , Al Qubeissi, M. , Kolodnytska, R. , Elwardany, A.E. , Nasiri, R. and Heikel, M.R. (2013) Modelling of biodiesel fuel droplet heating and evaporation. Fuel, volume 115 : 559–572. DOI: 10.1016/j.fuel.2013.07.031

http://dx.doi.org/10.1016/j.fuel.2013.07.031

Elsevier

Modelling of biodiesel fuel droplet heating and evaporation

S.S. Sazhin*[1], M. Al Qubeissi*, R. Kolodnytska•, A.E. Elwardany◇, R. Nasiri*, M.R. Heikal*,△

*Sir Harry Ricardo Laboratories, Centre for Automotive Engineering, School of Computing, Engineering and Mathematics, Faculty of Science and Engineering, University of Brighton, Brighton, BN2 4GJ, UK

•Department of Mechanical Engineering, Zhytomyr State Technological University, Chernyahovskogo, 103, Zhytomyr, 10005, Ukraine

◇Clean Combustion Research Centre, Division of Physical Sciences and Engineering, King Abdullah University of Science and Technology, Thuwal 23955-6900, Saudi Arabia

△Department of Mechanical Engineering, Universiti of Teknologies PETRONAS, Bandar Sri Iskandar 31750 Tronoh, Perak Darul Ridzuan, Malaysia

Abstract

Biodiesel fuel droplet heating and evaporation is investigated using the previously developed models, taking into account temperature gradient, recirculation, and species diffusion within droplets. The analysis is focused on four types of biodiesel fuels: Palm Methyl Ester, Hemp Methyl Esters, Rapeseed oil Methyl Ester, and Soybean oil Methyl Ester. These fuels contain up to 15 various methyl esters and possibly small amounts of unspecified additives, which are treated as methyl esters with some average characteristics. Calculations are performed using two approaches: 1) taking into account the contribution of all components of biodiesel fuels (up to 16); and 2) assuming that these fuels can be treated as a one component fuel with averaged transport and thermodynamic coefficients. It is pointed out that for all types of biodiesel fuel the predictions of the multi-component and single component models are rather close (the droplet evaporation times predicted by these models differ by less than about 5.5%). This difference is much smaller than observed in the case of Diesel and gasoline fuel droplets, and is related to the

[1]Corresponding author, e-mail: S.Sazhin@brighton.ac.uk

fact that in the case of Diesel and gasoline fuel droplets the contribution of components in a wide range of molar masses and enthalpies of evaporation needs to be taken into account, while in the case of biodiesel fuels the main contribution comes from the components in a narrow range of molar masses and enthalpies of evaporation. As in the case of Diesel and gasoline fuel droplets, the multi-component model predicts higher droplet surface temperature and longer evaporation times than the single component model.

Keywords:
Biodiesel fuel, methyl esters, multi-component droplets, heating, evaporation, modelling

---

1. Introduction

Depletion of fossil fuels and the need to reduce carbon dioxide emissions, contributing to climate changes, have stimulated the development of alternative fuels for internal combustion engines. As an alternative to Diesel fuel biodiesel fuels have been developed [1]. The term 'biodiesel' typically refers to "a fuel comprised of mono-alkyl esters of long-chain fatty acids derived from vegetable oils or animal fats" [2]. Sometimes it is used to refer to as "fatty acid methyl or ethyl esters made from vegetable oils or animal fats, whose properties are good enough to be used in diesel engines" [1]. Biodiesel is produced from vegetable oil or animal fat through the process known as transesterification [3]. Most studies of biodiesel fuels have been focused on rapeseed, soybean and palm oil biodiesels [5]. The dominant oils for production of these fuels are rapeseed oil in Europe, soybean oil in the USA, and palm oil in Asia [2]. The term 'second-generation biodiesel' refers to biodiesel derived from inedible oil or algae [4].

Our paper is focused on the modelling of biodiesel fuel droplet heating and evaporation, which is an important stage of the process leading from the injection of biodiesel fuel into a combustion chamber to its ultimate combustion, producing the driving force for internal combustion engines. A number of models of biodiesel fuel heating and evaporation of various complexities have been suggested (e.g. [6, 7]). These models either ignored temperature gradients and species diffusion inside droplets or took them into account based on the numerical solutions of the underlying partial differential equations (e.g. [7]). The importance of taking into account these effects has been discussed in a number of our previous papers, including [8, 9]. In

contrast to almost all previous investigations of these processes, the authors of [8, 9] based their analysis not on the numerical solutions of the equations for heat transfer and species diffusion in droplets, but on their analytical solutions, which were incorporated into a numerical algorithm.

This approach has been applied to the modelling of droplet heating and evaporation for binary mixtures and for simplified models of Diesel and gasoline fuels. The focus of our paper is on the application of this approach to modelling the heating and evaporation of droplets of various realistic biodiesel fuels in conditions typical for Diesel engines.

The model used in our analysis is briefly described in Section 2. The implementation of this model into a numerical algorithm is summarised in Section 3. Input parameters used in our analysis and the results of calculations are presented and discussed in Sections 4 and 5. The main results of the paper are summarised in Section 6.

2. The model

The main ideas of the model used in our analysis are rather similar to those behind the one described in [8]. This model takes into account the effects of multi-component droplet heating by convection, its evaporation, the finite thermal conductivity, recirculation, and species diffusion in the liquid phase. Only the effects of ambient gas on droplets are taken into account, the effects of coupling between gas and droplets are ignored (see [9] for a possible approach to describe this coupling).

2.1. Droplet heating

The process of heating of mono- and multi-component droplets is described by the following transient heat conduction equation for the temperature $T \equiv T(t, R)$ in the liquid phase [10, 11]:

$$\frac{\partial T}{\partial t} = \kappa \left(\frac{\partial^2 T}{\partial R^2} + \frac{2}{R} \frac{\partial T}{\partial R} \right), \tag{1}$$

where $\kappa = k_{\text{eff}}/(c_l \rho_l)$ is the effective thermal diffusivity, k_{eff}, c_l, and ρ_l are the effective thermal conductivity, specific heat capacity, and density respectively, R is the distance from the centre of the droplet (assumed to be spherical), t is time. k_{eff} is linked with the liquid thermal conductivity k_l via the following equation:

$$k_{\text{eff}} = \chi k_l, \tag{2}$$

where the coefficient χ varies from 1 (at droplet Peclet number $\mathrm{Pe}_{d(l)} = \mathrm{Re}_{d(l)}\mathrm{Pr}_l < 10$) to 2.72 (at $\mathrm{Pe}_{d(l)} > 500$) and can be approximated as [12]:

$$\chi = 1.86 + 0.86 \tanh\left[2.225 \log_{10}\left(\mathrm{Pe}_{d(l)}/30\right)\right]. \tag{3}$$

Liquid fuel transport properties and the liquid velocity just below the droplet surface (see [12] for details) were used for calculating $\mathrm{Pe}_{d(l)}$. The model based on Equations (2) and (3) is known as the Effective Thermal Conductivity (ETC) model. When writing Eq. (1) we assumed that droplet sphericity is not affected by its motion.

Equation (1) is to be solved for $t > 0$ and $0 \leq R < R_d$, where R_d is the droplet radius, with the following boundary condition, assuming that the effects of evaporation can be ignored:

$$h(T_g - T_s) = k_{\text{eff}} \left.\frac{\partial T}{\partial R}\right|_{R=R_d-0}, \tag{4}$$

and the initial condition $T(t=0) = T_{d0}(R)$, where $T_s = T_s(t)$ is the droplet's surface temperature, $T_g = T_g(t)$ is the ambient gas temperature, h is the convection heat transfer coefficient, linked with the Nusselt number Nu via the following equation:

$$\mathrm{Nu} = 2R_d h/k_g,$$

k_g is the gas thermal conductivity. We assume that fuel vapour is dilute and k_g is equal to the thermal conductivity of air. Remembering the physical background to the problem, we are interested only in a solution which is continuously differentiable twice in the whole domain. This implies that T should be bounded for $0 \leq R < R_d$.

Assuming that $h = \text{const}$, the solution to Equation (1), subject to the above boundary and initial conditions, can be presented as [13]:

$$T(R,t) = \frac{1}{R}\sum_{n=1}^{\infty}\left\{q_n \exp\left[-\kappa_R \lambda_n^2 t\right] - \frac{R_d^2 \sin\lambda_n}{||\ v_n\ ||^2\ \lambda_n^2}\mu_0(0)\exp\left[-\kappa_R\lambda_n^2 t\right]\right.$$

$$\left. - \frac{R_d^2 \sin\lambda_n}{||\ v_n\ ||^2\ \lambda_n^2}\int_0^t \frac{\mathrm{d}\mu_0(\tau)}{\mathrm{d}\tau}\exp\left[-\kappa_R\lambda_n^2(t-\tau)\right]\mathrm{d}\tau\right\}\sin\left[\lambda_n\left(\frac{R}{R_d}\right)\right] + T_g(t), \tag{5}$$

where λ_n are solutions to the equation:

$$\lambda\cos\lambda + h_0 \sin\lambda = 0, \tag{6}$$

$$|| v_n ||^2 = \frac{R_d}{2}\left(1 - \frac{\sin 2\lambda_n}{2\lambda_n}\right) = \frac{R_d}{2}\left(1 + \frac{h_0}{h_0^2 + \lambda_n^2}\right),$$

$$q_n = \frac{1}{|| v_n ||^2}\int_0^{R_d} \tilde{T}_0(R)\sin\left[\lambda_n\left(\frac{R}{R_d}\right)\right] \mathrm{d}R,$$

$$\kappa_R = \frac{k_{\text{eff}}}{c_l \rho_l R_d^2}, \qquad \mu_0(t) = \frac{hT_g(t)R_d}{k_{\text{eff}}},$$

$h_0 = (hR_d/k_{\text{eff}}) - 1$, $\tilde{T}_0(R) = RT_{d0}(R)$. The solution to Equation (6) gives a set of positive eigenvalues λ_n numbered in ascending order ($n = 1, 2, ...$). The trivial solution $\lambda = 0$ is not considered.

Note that the norm $|| v_n ||^2$ differs from the norm chosen in [13] by the factor R_d (see their Equation (A4)). This does not affect the final solution.

Solution (5) is valid for $h_0 > -1$, which is satisfied, remembering the physical background of the problem ($h > 0$). The condition h =const is valid for sufficiently small time steps.

To take into account the effect of droplet evaporation in analytical solution (5), gas temperature should be replaced by the so-called effective temperature defined as:

$$T_{\text{eff}} = T_g + \frac{\rho_l L \dot{R}_d}{h}, \tag{7}$$

where L is the latent heat of evaporation, the value of $\dot{R}_d$ can be taken from the previous time step and estimated based on Equation (28). R_d is assumed constant in the analytical solutions, but is updated at the end of the time step Δt:

$$R_{d(\text{new})} = R_{d(\text{old})} + \dot{R}_d \Delta t,$$

where the value of $\dot{R}_d$ is controlled by the droplet evaporation model (see Equation (28) in Section 2.3).

In the limit $k_{\text{eff}} \to \infty$ the prediction of Expression (5) is identical to the one which follows from the model based on the assumption that $k_{\text{eff}} = \infty$ [14] (Infinite Thermal Conductivity (ITC) model).

The value of Nu for an isolated moving droplet is estimated based on the following equation [12]:

$$\text{Nu}_{\text{iso}} = 2\frac{\ln(1 + B_T)}{B_T}\left(1 + \frac{(1 + \text{Re}_d\text{Pr}_d)^{1/3}\max\left[1, \text{Re}_d^{0.077}\right] - 1}{2F(B_T)}\right), \tag{8}$$

where

$$B_T = \frac{c_{pv}(T_g - T_s)}{L_{\text{eff}}}$$

is the Spalding heat transfer number,

$$F(B_T) = (1 + B_T)^{0.7} \frac{\ln(1 + B_T)}{B_T},$$

$L_{\text{eff}} = L + \frac{Q_L}{\dot{m}_d} = \sum_i \epsilon_i L_i + \frac{Q_L}{\sum_i \dot{m}_i}$, Q_L is the power spent on droplet heating, c_{pv} is the specific heat capacity of fuel vapour, $\epsilon_i = \epsilon_i(t)$ are the evaporation rates of species i, $\dot{m}_i = \epsilon_i \dot{m}_d$ ($\dot{m}_d = \sum_i \dot{m}_i$). The effects of the interaction between droplets are ignored.

2.2. Species diffusion in the liquid phase

Equations for mass fractions of liquid species $Y_{li} \equiv Y_{li}(t, R)$ inside moving but spherically symmetric droplets can be presented in the following form [8]:

$$\frac{\partial Y_{li}}{\partial t} = D_{\text{eff}} \left(\frac{\partial^2 Y_{li}}{\partial R^2} + \frac{2}{R} \frac{\partial Y_{li}}{\partial R} \right), \tag{9}$$

where $i = 1, 2, 3, ...$, D_{eff} is the effective mass diffusivity. D_{eff} is linked with the liquid diffusivity D_l via the following equation

$$D_{\text{eff}} = \chi_Y D_l, \tag{10}$$

where the coefficient χ_Y varies from 1 to 2.72 and can be approximated as:

$$\chi_Y = 1.86 + 0.86 \tanh \left[2.225 \log_{10} \left(\text{Re}_{d(l)} \text{Sc}_l / 30 \right) \right], \tag{11}$$

Sc_l is the liquid Schmidt number defined as:

$$\text{Sc}_l = \frac{\nu_l}{D_l}, \tag{12}$$

ν_l is the liquid kinematic viscosity. As in the case of k_{eff}, liquid fuel transport properties and the liquid velocity just below the droplet surface were used for calculating $\text{Re}_{d(l)}$. The model based on Equations (10) and (11) is known as the Effective Diffusivity (ED) model. The model, based on the assumption that species diffusivity is infinitely fast ($D_{\text{eff}} = \infty$) is referred to as the Infinite Diffusivity (ID) model. D_l is assumed to be the same for all species

(see Appendix 2 for details). The combined ITC/ID model is sometimes known as a well-mixed model.

Equation (9) is solved with the following boundary condition [8]:

$$\alpha(\epsilon_i - Y_{lis}) = -D_{\text{eff}} \left.\frac{\partial Y_{li}}{\partial R}\right|_{R=R_d-0}, \tag{13}$$

and the initial condition $Y_{li}(t=0) = Y_{li0}(R)$, where $Y_{lis} = Y_{lis}(t)$ are liquid components' mass fractions at the droplet's surface,

$$\alpha = \frac{|\dot{m}_d|}{4\pi\rho_l R_d^2}, \tag{14}$$

$\dot{m}_d$ is the droplet evaporation rate, the calculation of which is discussed in the next subsection (see Equation (19)).

As in the case of Equation (1), we are interested only in a solution which is continuously differentiable twice in the whole domain. This implies that Y_{li} should be bounded for $0 \le R \le R_d$. Moreover, the physical meaning of Y_{li}, as the mass fraction, implies that $0 \le Y_{li} \le 1$.

Assuming that species concentrations in the ambient gas are equal to zero, the values of ϵ_i can be found from the following relation [8]:

$$\epsilon_i = \frac{Y_{vis}}{\sum_i Y_{vis}}, \tag{15}$$

where the subscript $_v$ indicates the vapour phase. The condition $\alpha = \text{const}$ can always be guaranteed for sufficiently small time steps.

The analytical solution to Equation (9) in this case can be presented as [8]:

$$Y_{li} = \epsilon_i + \frac{1}{R}\left\{\left[\exp\left[D_{\text{eff}}\left(\frac{\lambda_0}{R_d}\right)^2 t\right][q_{i0} - Q_0\epsilon_i]\sinh\left(\lambda_0\frac{R}{R_d}\right)\right.\right.$$
$$\left.\left. + \sum_{n=1}^{\infty}\left[\exp\left[-D_{\text{eff}}\left(\frac{\lambda_n}{R_d}\right)^2 t\right][q_{in} - Q_n\epsilon_i]\sin\left(\lambda_n\frac{R}{R_d}\right)\right]\right\}, \tag{16}$$

where λ_0 and λ_n $(n \ge 1)$ are solutions to equations

$$\tanh\lambda_0 = -\frac{\lambda_0}{h_{0Y}} \quad \text{and} \quad \tan\lambda_n = -\frac{\lambda_n}{h_{0Y}} \ \ (n \ge 1)$$

respectively, $h_{0Y} = -\left(1 + \frac{\alpha R_d}{D_{\text{eff}}}\right)$.

$$Q_n = \begin{cases} -\frac{1}{||v_0||^2}\left(\frac{R_d}{\lambda_0}\right)^2 (1 + h_{0Y}) \sinh \lambda_0 & \text{when} \quad n = 0 \\ \frac{1}{||v_n||^2}\left(\frac{R_d}{\lambda_n}\right)^2 (1 + h_{0Y}) \sin \lambda_n & \text{when} \quad n \geq 1 \end{cases} \tag{17}$$

$$q_{in} = \frac{1}{||v_n||^2} \int_0^{R_d} R Y_{li0}(R) v_n(R) \mathrm{d}R, \tag{18}$$

$n \geq 0$, where

$$v_0(R) = \sinh\left(\lambda_0 \frac{R}{R_d}\right), \quad v_n(R) = \sin\left(\lambda_n \frac{R}{R_d}\right), \ \ n \geq 1.$$

When considering the diffusion of several species it is assumed that D_{eff} is the same for all species and that it can be estimated based on the average characteristics of biodiesel fuel (see Appendix 2 for details). This model is known as the Discrete Component Model (DCM).

For modelling multi-component droplet heating and evaporation, with many species involved, a new model, called the quasi-discrete model was suggested and developed in [15, 16, 17]. This model is based on the introduction of quasi-components, describing groups of actual components with close properties. In contrast to the previously suggested models, designed for large numbers of components, the new model takes into account the diffusion of liquid quasi-components and thermal diffusion as in the classical DCM. This approach will not be used in our model since we cannot easily introduce a distribution function with respect to the number of carbon atoms required. The limited number of components to be involved in the analysis (not more than 16) can be dealt with using the classical DCM.

2.3. Droplet evaporation

In the case of isolated moving mono-component droplets, their evaporation rate is given by the following equation [18]:

$$\dot{m}_d = -2\pi R_d D_v \rho_{\text{total}} B_M \text{Sh}_{\text{iso}}, \tag{19}$$

where D_v is the binary diffusion coefficient of vapour in air, B_M is the Spalding mass transfer number defined as:

$$B_M = \frac{\rho_{vs} - \rho_{v\infty}}{\rho_{gs}} = \frac{Y_{vs} - Y_{v\infty}}{1 - Y_{vs}}, \tag{20}$$

Y_v is the vapour mass fraction, $\mathrm{Sh}_{\mathrm{iso}}$ is the Sherwood number approximated for the isolated droplets by the following expression:

$$\mathrm{Sh}_{\mathrm{iso}} = 2\frac{\ln(1+B_M)}{B_M}\left(1+\frac{(1+\mathrm{Re}_d\mathrm{Sc}_d)^{1/3}\max\left[1,\mathrm{Re}_d^{0.077}\right]-1}{2F(B_M)}\right), \quad (21)$$

$$\mathrm{Sc}_d = \frac{\nu_{\mathrm{air}}}{D_v}$$

is the Schmidt number,

$$F(B_M) = (1+B_M)^{0.7}\frac{\ln(1+B_M)}{B_M}.$$

B_T and B_M are linked by the following equation [12]:

$$B_T = (1+B_M)^{\varphi} - 1, \quad (22)$$

where

$$\varphi = \left(\frac{c_{pv}}{c_{pa}}\right)\left(\frac{\mathrm{Sh}^*}{\mathrm{Nu}^*}\right)\frac{1}{\mathrm{Le}}, \quad (23)$$

$\mathrm{Le} = k_g/(c_{pa}\rho_{\mathrm{total}}D_v) = \mathrm{Sc}_d/\mathrm{Pr}_d$ is the Lewis number,

$$\mathrm{Sh}^* = 2\left(1+\frac{(1+\mathrm{Re}_d\mathrm{Sc}_d)^{1/3}\max\left[1,\mathrm{Re}_d^{0.077}\right]-1}{2F(B_M)}\right), \quad (24)$$

$$\mathrm{Nu}^* = 2\left(1+\frac{(1+\mathrm{Re}_d\mathrm{Pr}_d)^{1/3}\max\left[1,\mathrm{Re}_d^{0.077}\right]-1}{2F(B_T)}\right). \quad (25)$$

As follows from Eq. (23), φ is a function of B_T. Hence, the iteration process needs to be performed to calculate B_T from Eq. (22). In our previous paper [19] it was shown that in some practically important cases, Formula (23) can be simplified assuming that $\frac{\mathrm{Sh}^*}{\mathrm{Nu}^*} = 1$. This assumption turned out to be too crude in our case.

In the case of multi-component droplets, the problem of modelling droplet evaporation is complicated by the fact that different species diffuse at different rates, and the evaporation rate of one of the species is affected by the evaporation rate of other species. In [20] the analysis of evaporation of multi-component droplets led to the following expression for $\dot{m}_d$:

$$\dot{m}_d = -2\pi R_d D_{iv}\rho_{\mathrm{total}}B_{Mi}\mathrm{Sh}_{\mathrm{iso}\,(i)}, \quad (26)$$

where B_{Mi} is the species Spalding mass transfer number defined as:

$$B_{Mi} = \frac{Y_{ivs} - Y_{iv\infty}}{\epsilon_i - Y_{ivs}}, \tag{27}$$

D_{iv} is the diffusion coefficient of species i in air, $\mathrm{Sh}_{\mathrm{iso}\,(i)}$ was defined by (21) replacing B_M with B_{Mi}. Remembering (15) one can see that $B_M = B_{Mi}$. Hence, for stationary droplets this leads to the paradox that the same value of $\dot{m}_d$ is predicted by Equation (26) for different D_{iv}. This paradox is resolved by the fact that, although Equation (26) is correct, the value of $\mathrm{Sh}_{\mathrm{iso}\,(i)}$ cannot be approximated by the analogue of Equation (21) which is implicitly based on the assumption that the evaporating species do not affect each other.

Our analysis of $\dot{m}_d$ is based on Equation (19), assuming that the mixture of vapour species can be treated as a separate gas, similar to treating the mixture of nitrogen, oxygen and carbon dioxide as air ($Y_{vs} = \sum_i Y_{vis}$). The value of D_v is estimated as described in Appendix 2.

When calculating the value of $\dot{R}_d$ we took into account both droplet evaporation during the time step, and the change in their density during this time step (see Equation (20) in [21]):

$$\dot{R}_d = \frac{\dot{m}_d}{4\pi R_d^2 \rho_l} + \frac{R_d(\overline{T}_0)}{\Delta t}\left[\left(\frac{\rho(\overline{T}_0)}{\rho(\overline{T}_1)}\right)^{1/3} - 1\right], \tag{28}$$

where $\overline{T}_0$ and $\overline{T}_1$ are average droplet temperatures at the beginning $t = t_0$ and the end of the time step $t = t_1$, $\Delta t = t_1 - t_0$.

2.4. Species mass fractions at the surface of the droplets

To calculate the species mass evaporation rate $\dot{m}_i$ and the values of the normalised evaporation rate of species ϵ_i, based on Equation (15), we need to calculate first the values of Y_{vsi}. The latter depends on the partial pressure of species i in the vapour state in the immediate vicinity of the droplet surface [22]:

$$p_{vsi} = X_{lsi}\gamma_i p^*_{vsi}, \tag{29}$$

where X_{lsi} is the molar fraction of the ith species in the liquid near the droplet surface, p^*_{vsi} is the partial vapour pressure of the ith species in the case when $X_{lsi} = 1$, γ_i is the activity coefficient. In the limit when $\gamma_i = 1$, Equation (29) describes Raoult's law. This law is assumed to be valid in our

analysis. Approximations for p^*_{vsi} are discussed in Appendix 2. Note that $p^*_{vsi} = p_v(R_d)$ for the ith species.

All liquid properties are calculated for the average temperature inside droplets. All gas properties are calculated for the reference temperature $T_r = (2/3)T_s + (1/3)T_g$, where T_s and T_g are droplet surface and ambient gas temperatures respectively. Enthalpy of evaporation and saturated vapour pressure are estimated at the surface temperature T_s.

3. Numerical algorithm

These are the main steps of the numerical algorithm:

1. Consider the initial distribution of temperature and mass fractions of species inside the droplet or use the distributions obtained at the previous time step (in the case of initial distributions, both are assumed homogeneous). Recalculate the molar fractions of species into mass fractions of species based on Eq. (46).

2. Calculate the values of transport and thermodynamic properties, including liquid thermal conductivity and effective thermal conductivity of the droplet.

3. Calculate species partial pressures and molar fractions in the gas phase using Equation (29).

4. Assuming that the concentration of vapour of all species in the ambient gas can be ignored, calculate the value of the Spalding mass transfer number, using Equation (20).

5. Calculate the values of heat capacity, diffusivity of the mixture of vapour species in the air and species evaporation rates (ϵ_i).

6. Calculate the value of the Spalding heat transfer number based on Equation (22) using the iteration process.

7. Calculate the values of Nusselt and Sherwood numbers for isolated droplets using Equations (8) and (21).

8. Calculate the rate of change of droplet radius using Equation (28).

9. Calculate the effective temperature using Equation (7).

10. Calculate the distribution of temperature inside the droplet based on Equation (5), using 33 terms in the series.

11. Calculate the distribution of species inside the droplet based on Equation (16), using 33 terms in the series. Note that the chosen number of terms visibly affects the predicted distribution of species if this number is much

lower than 33. This effect is much weaker for the distribution of temperature in droplets.

12. Recalculate the droplet's radius at the end of the time step Δt. If this radius is negative then the time step is reduced and the calculations are repeated. If the ratio of this radius to the initial radius is less than an *à priori* chosen small number $\varepsilon_s = 10^{-6}$ then the remaining part of the droplet is assumed to be evaporated with all liquid species transferred into the gas phase with the corresponding decrease in gas temperature. If this ratio is greater than 10^{-6} then go to the next step.

13. Recalculate the distributions of temperature and species for the new radius (e.g. $T(R) = T(R\,R_{d2}/R_{d1}) = T(\tilde{R})$, where $R_{d1,2}$ are droplet radii at the beginning and the end of the time step, $\tilde{R}$ is the new R used at the second time step, T are the values of temperature at the end of the first time step).

14. Return to Step 1 and repeat the calculations for the next time step.

4. Input parameters

The Sauter Mean Diameters (SMD) of biodiesel fuel droplets at temperature 80°C, as reported by [23, 24], are shown in Table 1.

Reference	**PME**	**HME1**	**HME2**	**RME**	**SME**
[23]	25.1 μm	-	-	28.8 μm	25.7 μm
[24]	-	23.55 μm	23.55 μm	26.69 μm	23.87 μm

Table 1

Various types of biodiesel fuels, mentioned in Table 1, are described in Appendix 1.

As can be seen from Table 1, the values of the SMDs for all five biodiesel fuels turned out to be rather close with the average value of SMD equal to 25.32 μm. In our further analysis it is assumed that the initial values of droplet radii are equal to $R_{d0} = 12.66$ μm.

Note that the same authors [23, 24] reported that the SMDs of Diesel fuel droplets, for the same conditions as those used for Table 1 (17.7 μm [23] and 18.3 μm [24]), are lower than those of biodiesel fuel droplets shown in Table 1. This can be attributed to the fact that the higher viscosity of biodiesel

fuel leads to lower jet velocity and larger droplet sizes compared with Diesel fuel [25].

As reported by [26], the initial droplet temperatures could vary from 375 K to 440 K. In our analysis, we assume that $T_{d0} = 375$ K.

As to the ambient air parameters, the following ranges of air density and temperature were reported in [26] for biofuels: 3.3 – 60 kg/m^3 and 700 – 1300 K. If we assume that the ideal gas law is valid this corresponds to the following range of air pressures: 6.63 – 223.9 bar (assuming that the gas constant for air is equal to 287 J/(kg K)). Near the upper limits of these parameters, the analysis would require the application of the equation of state for real gases which is beyond the scope of this paper. Our analysis is focused on the same values of parameters as in [15] for Diesel engine conditions (assuming that the ideal gas law is valid):

$$\rho_a = 11.9\,\mathrm{kg/m^3}, \quad T_a = 880\,\mathrm{K}, \quad p_a = 30\,\mathrm{bar}.$$

These values are compatible with, although slightly lower than those reported [26].

5. Results

Molar fractions of components of biodiesel fuel used in our analysis are shown in Table A1. Using the values of the input parameters described in the previous section, the thermodynamic and transport properties of components described in Appendix 2, the Effective Thermal Conductivity/Effective Diffusivity (ETC/ED) model, and assuming that droplets are stationary ($v_d = 0$), the values of droplet surface temperature (T_s) and radius (R_d) versus time (t) have been calculated for all 5 types of biodiesel fuels shown in Table A1. The calculations have been performed: 1) taking into account the contribution of up to 16 components shown in Table A1 (multi-component models); and 2) replacing these components by a single component with average transport and thermodynamic properties obtained as described in Appendix 3 (single component models).

The results for PME are shown in Fig. 1. As follows from this figure, the multi-component model predicts higher droplet surface temperatures and longer evaporation times compared with the single component model. This result is consistent with the one earlier reported in [15, 16, 17] for Diesel and gasoline fuel droplets. As in the case of the abovementioned fuels, this

behaviour of the droplet surface temperature and radius can be related to the fact that at the final stages of droplet evaporation the mass fraction of species with larger numbers of carbon atoms n (C20:1 M, C18:1 M, C18:2 M, C18:0 M) increases at the expense of species with smaller n (C16:0 M) except at the very final stage of droplet evaporation. At this final stage, for all species except C20:1 M, the mass fraction starts to decrease. This is demonstrated in Fig. 2, where the time evolution of surface mass fractions of four dominant species is presented. The behaviour of surface mass fractions of the intermediate species (C18:1 M, C18:2 M, C18:0 M) when their mass fractions first increase and then start to decrease at the final stage of droplet heating and evaporation is similar to that observed for Diesel and gasoline fuel droplets (cf. Fig. 11 of [16]). The species with larger n evaporate more slowly than the species with lower n and have higher wet bulb temperatures.

The plots of mass fractions of two dominant species in PME droplets (C16:0 M and C18:1 M) versus normalised radius R/R_d at three instants of time (0.3 ms, 1 ms and 2 ms) are shown in Fig. 3. At $t = 0$ these plots are the lines parallel to the R/R_d axis. As one can see from this figure, at all three time instants the mass fractions of both components remain rather close to their initial values near the droplet centre, but the difference between them increases in the region close to the droplet surface, especially at $t = 2$ ms. The values of these mass fractions at the droplet surface are the same as those shown in Fig. 2.

The plots of temperatures in PME droplets versus normalised distance from the centre of the droplet R/R_d at five instants of time (0.02 ms, 0.3 ms, 0.5 ms, 1 ms and 2 ms) are shown in Fig. 4. At $t = 0$ the plot reduces to the line parallel to the R/R_d axis ($T = 375$ K). As one can see from this figure the heating of the surface of the droplet is noticeable at very early times ($t = 0.03$ ms), while the gradient of temperature inside the droplet can be seen at all times up to $t = 2$ ms (approximately 60% of the evaporation time). This demonstrates the limitation of the widely used Infinite Thermal Conductivity (ITC) model, in agreement with our earlier results [8, 9, 15, 16].

Note that the difference between the values of droplet surface temperatures (T_s) and radii (R_d) predicted by the multi-component and single component models is much smaller for PME than for Diesel and gasoline fuels (cf. Figs. 2, 5 and 8 of [16]). The droplet evaporation times predicted by these models for PME droplets differ by 2.10% (relative to the prediction of the single component model). This can be related to the fact that in PME the dominant components have relatively close molar masses and correspond-

ing boiling temperatures and enthalpies of evaporation, while in the case of Diesel and gasoline fuels the contributions of components in a wide range of molar masses, boiling temperatures and enthalpies of evaporation need to be taken into account. This implies that the approximation of PME with a single component is expected to be much more accurate compared with the case of Diesel and gasoline fuels.

The plots similar to those shown in Fig. 1 but for HME1, are presented in Fig. 5. Comparing Figs. 1 and 5 one can see that HME1 droplets evaporate for slightly longer than PME droplets and the surface temperatures of HME1 droplets, predicted by the multi-component model at the final stage of droplet evaporation, are slightly higher than the ones predicted for the PME droplets. Apart from these remarks, the difference between the predictions of the multi-component and single component models for HME1 is rather similar to that for PME. However, the processes which take place in HME1 and PME droplets are rather different. This is demonstrated in Fig. 6, which shows the time evolution of surface mass fractions of five dominant species. The species with larger n (C24:0 M) evaporate more slowly than the species with smaller n (C18:2 M, C18:3 M, C18:1 M and C16:0 M) and have higher wet bulb temperatures. This leads to an increase in the surface mass fraction of C24:0 M at the final stage of droplet heating and evaporation at the expense of the surface mass fractions of C18:2 M, C18:3 M, C18:1 M and C16:0 M. The plots of mass fractions of species and temperatures in HME1 droplets versus normalised distance from the centre of the droplet R/R_d at various instants of time show the same trends as in the case of PME. These plots are not presented.

The plots similar to those shown in Figs. 1 and 5 but for HME2, are presented in Fig. 7. The latter plots are rather similar to those referring to HME1, except that the results predicted by multi-component and single component models are much closer for HME2 than for HME1. The droplet evaporation times predicted by these models differ by 0.58%. This can be explained by the fact that there are no heaviest components (C22:1 M and C24:1 M) in HME2 while they are quite noticeable in HME1 (see Table A1). The time evolution of surface mass fractions of five dominant species in HME2 droplets is shown in Fig. 8. As one can see in this figure, the mass fraction of the heaviest component C20:0 M increases with time at the final stage of droplet evaporation, while mass fractions of all other components decrease with time. These decreases and increases are less pronounced compared with the cases shown in Figs. 2 and 6, which is reflected in the closeness

of the droplet surface temperatures and radii predicted by multi-component and single component models. The plots of mass fractions of species and temperatures in HME2 droplets versus normalised distance from the centre of the droplet R/R_d at various instants of time show the same trends as in the case of PME and HME1. These plots are not presented.

The plots similar to those shown in Figs. 1, 5 and 7 but for RME, are presented in Fig. 9. The plots shown in this figure are rather similar to those referring to previously considered biodiesel fuels, except that the deviation between the results predicted by multi-component and single component models is larger than in the case of PME, HME1 and HME2. The droplet evaporation times predicted by these models for RME differ by 5.50%. This can be attributed to the presence in RME of two components, C22:1 M and C18:2 M, with almost equal initial mass fractions, but different molar masses, boiling temperatures and enthalpies of evaporation. The mass fractions of species with larger n (C22:1 M and C24:1 M) increase at the expense of species with smaller n (C16:0 M, C18:1 M, C18:2 M and C18:3 M) except at the very final stage of droplet evaporation. At this final stage all species except C24:1 M start to decrease. This is demonstrated in Fig. 10, where the time evolution of surface mass fractions of six dominant species is presented. As in the case of previously considered biodiesel fuels, the species with larger n evaporate more slowly than the species with lower n and have higher wet bulb temperatures. The plots of mass fractions of species and temperatures in RME droplets versus normalised distance from the centre of the droplet R/R_d at various instants of time show the same trends as in the case of PME, HME1 and HME2. These plots are not presented.

The plots similar to those shown in Figs. 1, 5, 7 and 9 but for SME, are presented in Fig. 11. The plots shown in this figure are rather similar to those referring to previously considered biodiesel fuels, especially those for HME1. The droplet evaporation times predicted by these models differ by 1.16%. The time evolution of surface mass fractions of six dominant species in SME droplets is shown in Fig. 12. As one can see in this figure, the mass fraction of the heaviest component, C22:1 M, increases with time at the final stage of droplet evaporation, while mass fractions of all other components decrease with time. These decreases and increases are less pronounced compared with the cases shown in Fig. 10, which is reflected in the relative closeness of the droplet surface temperatures and radii predicted by multi-component and single component models. The plots of mass fractions of species and temperatures in SME droplets versus normalised radius R/R_d at various

instants of time show the same trends as in the case of PME, HME1, HME2 and RME. These plots are not presented.

The plots for the same case as shown in Fig. 1, but for a droplet moving with velocity 10 m/s, are presented in Fig. 13. In the same figure, the plots calculated using the multi-component model, based on the Infinite Thermal Conductivity/Infinite Diffusivity (ITC/ID) approach, are shown. Comparing Figs. 1 and 13 one can see that moving droplets evaporate about 3 times faster than stationary droplets as expected. As in the case of Diesel and gasoline fuel droplets [15, 16], there are noticeable differences in predictions based on the ETC/ED and ITC/ID models, especially for temperatures at the initial stage of droplet heating. As mentioned in [15, 16] accurate prediction of these temperatures is particularly important for the prediction of the auto-ignition timing in Diesel engines. This brings into question the reliability of the models for heating and evaporation of biodiesel droplets, based on the ITC/ID approximations. These models are almost universally used for the analysis of these processes. As in the case shown in Fig. 1, the multi-component model predicts higher droplet surface temperatures and longer evaporation times compared with the single component model. The droplet evaporation times predicted by these models differ by 1.6 %. This difference between the predictions of these models is slightly smaller than in the case of stationary droplets.

6. Conclusions

The previously suggested model for droplet heating and evaporation, taking into account temperature gradient and recirculation inside droplets and species diffusion within them, has been applied to the analysis of biodiesel fuel droplet heating and evaporation in realistic Diesel engine-like conditions. In contrast to most commonly used models to take into account these effects, our model is based on the analytical solutions to the heat transfer and species diffusion equations inside droplets. The analysis has been focused on five types of biodiesel fuels: Palm Methyl Ester (PME) produced from palm oil, Hemp Methyl Esters, produced from hemp seed oil in the Ukraine (HME1) and European Union (HME2), Rapeseed oil Methyl Ester (RME), produced from rapeseed oil in the Ukraine, and Soybean oil Methyl Ester (SME) produced from soybean oil. These fuels contain up to 15 methyl esters and possibly small amounts of unspecified additives, which are treated as methyl esters with average characteristics.

Calculations have been performed: 1) taking into account the contribution of all components of biodiesel fuel; and 2) assuming that this fuel can be treated as a one component fuel with averaged transport and thermodynamic coefficients (as a widely used approximation for the analysis of realistic multi-component fuels, including biodiesel fuels). It has been pointed out that for HME2 the droplet surface temperatures and radii predicted by the multi-component and single component models almost coincide, which justifies the application of the single component model for the analysis of droplet heating and evaporation. For PME, HME1 and SME the predictions of the multi-component and single component models were rather close (the droplet evaporation times predicted by these models differ by less than about 2%). The maximal deviation between the predictions of the multi-component and single component models have been observed for RME. Even in the latter case, however, the difference between the evaporation times predicted by these models has been less than about 5.5%. This difference is much smaller than observed in the case of Diesel and gasoline fuel droplets (see Figs. 2, 5 and 8 in [16]).

This difference in the predictions of biodiesel, Diesel and gasoline droplet heating and evaporation is related to the fact that in the case of Diesel and gasoline droplets the contribution of components in a wide range of molar masses, boiling temperatures and enthalpies of evaporation needs to be taken into account, while in the case of biodiesel droplets the main contribution comes from the components in a narrow range of molar masses, boiling temperatures and enthalpies of evaporation. As in the case of Diesel and gasoline droplets, for biodiesel droplets the multi-component model predicts higher droplet surface temperatures and longer evaporation times than the single component model. This is related to the fact that at the final stages of droplet evaporation the mass fraction of heavier species increases at the expense of lighter species. The heavier species evaporate more slowly than the lighter species and have higher wet bulb temperatures.

Acknowledgments

The authors are grateful to Paul Harris for useful discussions, and the Ministry of Education of the Ukraine and the EPSRC (grant EP/J006793/1) for their financial support of the work on this project.

Appendix 1

Composition of biodiesel fuels

The following biodiesel fuels are used in our analysis: Palm Methyl Ester (PME) produced from palm oil [27], Hemp Methyl Esters, produced from hemp seed oil in the Ukraine (HME1) [24] and European Union (HME2) [28], Rapeseed oil Methyl Ester (RME) [5], produced from rapeseed oil in the Ukraine, and Soybean oil Methyl Ester (SME) produced from soybean oil [29]. Molar fractions of components (pure methyl esters) of these fuels are shown in Table A1.

Component	**PME**	**HME1**	**HME2**	**RME**	**SME**
C12:0 M	0.0026	0.0000	0.0000	0.0000	0.0000
C14:0 M	0.0129	0.0000	0.0000	0.0000	0.0000
C16:0 M	0.4513	0.0662	0.0651	0.0495	0.109
C17:0 M	0.0000	0.0021	0.0000	0.0000	0.0000
C18:0 M	0.0447	0.0206	0.0246	0.0167	0.044
C20:0 M	0.0035	0.0045	0.0090	0.0056	0.004
C22:0 M	0.0000	0.0025	0.0000	0.0000	0.0000
C24:0 M	0.0000	0.0023	0.0000	0.0000	0.0000
C16:1 M	0.0021	0.0033	0.0000	0.0000	0.0000
C18:1 M	0.3839	0.1188	0.1188	0.2671	0.240
C20:1 M	0.0017	0.0027	0.0090	0.0000	0.0000
C22:1 M	0.0000	0.0017	0.0000	0.2204	0.003
C24:1 M	0.0000	0.0015	0.0000	0.0077	0.0000
C18:2 M	0.0916	0.5671	0.5482	0.2484	0.528
C18:3 M	0.0019	0.2067	0.2007	0.0973	0.072
Other	0.0038	0.0000	0.0246	0.0873	0.0000

Table A1

Chemical formulae of the components presented in Table A1, their names and their molar masses are shown in Table A2 [30]. The numbers of carbons in fatty acids (n_{acid}) and numbers of double bonds (DB) in each component are shown by the numbers on the left and on the right of ':' respectively in the expressions for the components. For example, C16:1 M has $n_{\text{acid}} = 16$

and DB= 1. The total number of carbon atoms in methyl esters is equal to $n_{\text{acid}} + 1$. Note that an alternative name for 'Methyl dodecanoate' is 'Methyl laurate', for 'Methyl tetradecanoate' is 'Methyl myristate', and for 'Methyl decosanoate' is 'Methyl behenate'.

Comp.	Chem. form.	Name	Mol. mass (kg/kmol)
C12:0 M	$C_{13}H_{26}O_2$	Methyl dodecanoate	214.338
C14:0 M	$C_{15}H_{30}O_2$	Methyl tetradecanoate	242.39
C16:0 M	$C_{17}H_{34}O_2$	Methyl palmitate	270.442
C17:0 M	$C_{18}H_{36}O_2$	Methyl heptadecanoate	284.468
C18:0 M	$C_{19}H_{38}O_2$	Methyl stearate	298.494
C20:0 M	$C_{21}H_{42}O_2$	Methyl eicosanoate	326.546
C22:0 M	$C_{23}H_{46}O_2$	Methyl decosanoate	354.598
C24:0 M	$C_{25}H_{50}O_2$	Methyl tetracosanoate	382.65
C16:1 M	$C_{17}H_{32}O_2$	Methyl palmitoleate	268.426
C18:1 M	$C_{19}H_{36}O_2$	Methyl oleate	296.478
C20:1 M	$C_{21}H_{40}O_2$	Methyl eicosenoate	324.53
C22:1 M	$C_{23}H_{44}O_2$	Methyl erucate	352.582
C24:1 M	$C_{25}H_{48}O_2$	Methyl nervonate	380.634
C18:2 M	$C_{19}H_{34}O_2$	Methyl linoleate	294.462
C18:3 M	$C_{19}H_{32}O_2$	Methyl linolenate	292.446
Other			298.111

Table A2

As follows from Table A1, the contribution of other components to biodiesel fuels varies from 0 to about 2.5% and can be considered very small. Since the composition of these other components has not been reported in the above-mentioned papers, we believe that it would be reasonable to assume that all parameters of these other components, including molar masses shown in Table A2, can be calculated as an arithmetic average of the corresponding values for all remaining components from C12:0 M to C18:3 M.

Chemical structures of three typical components shown in Tables A1 and A2 (C18:0 M, C18:1 M, C18:2), illustrating the meaning of DB, are shown in Fig. A1.

Appendix 2

Transport and thermodynamic properties of the components of biodiesel fuels

All values of parameters in this section are given in SI units. For temperatures above the upper limit of the validity of formulae given below it is assumed that the corresponding transport and thermodynamic properties are equal to those at the upper limit temperatures, unless specified otherwise.

Liquid density

The density of pure liquid methyl esters shown in Tables A1 and A2 can be estimated based on the following general formula [33]:

$$\rho_l = \rho_{l0} - \alpha_T (T - 288.15), \tag{30}$$

where

$$\rho_{l0} = 851.471 + \frac{250.718\,\mathrm{DB} + 280.899}{1.214 + n_{\mathrm{acid}}},$$

$$\alpha_T = \frac{7.536}{\ln(n_{\mathrm{acid}}) + 3.584} - 0.446,$$

n_{acid} is the number of carbons in fatty acids, DB is the number of double bonds. The lower limit of applicability of Eq. (30) was extended up to 288.15 K (15 °C), while the upper limit of their applicability was not investigated in [33]. However, based on the results presented in [31] we can anticipate that the linear dependence of liquid density on temperature is maintained from room temperature up until the vicinity of the critical temperature with about the same regression rate. This allows us to use this equation from 288.15 K to the critical temperature. It is anticipated that at temperatures close to the critical temperature, if this range of temperatures is reached, the droplets become close to being completely evaporated and the errors in estimating droplet densities will produce negligible effect on the overall droplet evaporation time.

Liquid viscosity

For saturated methyl esters (with zero double bonds, DB=0) the liquid kinematic viscosity can be estimated based on the following formula, valid in the temperature range 293.15 K $\leq T \leq$ 353.15 K [34]:

$$\ln\left[\nu_l \times 10^6\right] = -2.177 - 0.202\, n_{\mathrm{acid}} + \frac{403.66}{T} + \frac{109.77\, n_{\mathrm{acid}}}{T}. \tag{31}$$

Formula (31) can still be used at temperatures above 353.15 K, although with lower accuracy [34]. Remembering that the final results are not very sensitive to the values of ν_l, this formula is used in the temperature range 293.15 K $\leq T \leq$ min(700 K, $T_{\rm cr}$). Note that for the processes considered in our paper the droplet temperatures almost never exceed 700 K.

For unsaturated methyl esters (with non-zero double bonds, DB$\geq$ 1) the liquid kinematic viscosity can be estimated based on the following formula, valid in temperature range $T \leq 0.7\,T_{\rm cr}$ [31, 35]:

$$\ln \frac{\nu_l \rho_l 10^6}{\rho_{l(20)} M} = A_k + \frac{B_k}{T}, \tag{32}$$

where $\rho_{l(20)}$ is liquid density at $T = 293.15$ K, M are molar masses given in Table A2. Coefficients A_k and B_k are given in Table A3.

Coefficient	C16:1 M – C24:1 M	C18:2 M	C18:3 M
A_k	-10.83	-9.93	-9.03
B_k	2099	1721	1343

Table A3

Liquid thermal conductivity and latent heat of evaporation

The thermal conductivity of pure liquid methyl esters shown in Tables A1 and A2 can be estimated based on the following general formula (Latini method) [36, 37, 38]:

$$k_l = \frac{0.0415\, T_b^{1.2}\,(1 - T_r)^{0.38}}{M\; T_{\rm cr}^{0.167}\; T_r^{1/6}}, \tag{33}$$

where

$$T_r = \frac{T}{T_{\rm cr}},$$

the values of the boiling and critical temperatures (T_b and $T_{\rm cr}$) for methyl esters used in our study are estimated from the following expressions [6]:

$$T_b = a_b + b_b M, \tag{34}$$

$$T_{\rm cr} = a_{\rm cr} + b_{\rm cr} M, \tag{35}$$

the values of coefficients in Eqs. (34) and (35) for various pure methyl esters are given in Table A4.

Coefficient	C12:0 M – C24:0 M	C16:1 M – C24:1 M	C18:2 M	C18:3 M
a_b	348.7	350.4	352.1	353.82
b_b	0.8478	0.8463	0.8463	0.8472
$a_{\rm cr}$	534.3	538.5	542.6	546.8
$b_{\rm cr}$	0.784	0.777	0.772	0.7711
a_L	1.506×10^7	1.389×10^7	1.270×10^7	1.154×10^7
b_L	1.814×10^5	1.822×10^5	1.834×10^5	1.843×10^5

Table A4

The calculation of the thermal conductivity of the mixture of components forming biodiesels presented in Table A1 led to its noticeable (up to 50%) under-estimation compared with experimentally observed values. This under-estimation could possibly be attributed to the low accuracy of the estimation of the coefficient 0.0415 for methyl esters. We were able to demonstrate that replacing this coefficient with 0.0713 led to much better agreement with experimental data for the mixtures. This leads to the modification of Eq. (33) to

$$k_l = \frac{0.0713\, T_b^{1.2}\, (1 - T_r)^{0.38}}{M\, T_{\rm cr}^{0.167}\, T_r^{1/6}}. \tag{36}$$

The method of estimation of thermal conductivity based on (36) is called the modified Latini method. The results predicted by (36) have been validated based on experimental data presented in [39, 40].

The molar latent heat of evaporation of pure methyl esters shown in Tables A1 and A2 is estimated based on the following general formula, valid in temperature range 300 K $\leq T \leq$ 700 K [6, 41]:

$$L = (a_L + b_L M)\, \Phi_L, \tag{37}$$

where

$$\Phi_L = \left(\frac{T_{\rm cr} - T}{T_{\rm cr} - T_b} \right)^{0.38}, \tag{38}$$

the values of coefficients in Eqs. (34), (35) and (37) for various pure methyl esters are given in Table A4. Note that coefficients for C18:3 M have been

obtained via the linear extrapolation of the values of the coefficients for C18:1 M and C18:2 M.

Although the coefficients in (37) have been obtained for 300 K $\leq T \leq$ 700 K, this formula is used in our analysis for temperatures up to the critical temperature to allow us to capture zero L at the critical temperature. This assumption has no practical importance in our analysis as droplet surface temperatures in our calculations have not exceeded 700 K in almost all cases.

Numerical values of the parameter $(T_{\rm cr}-T_b)^{0.38}$ were used in [6] to simplify calculations based on Eq. (38).

Liquid heat capacity

The specific heat capacities (in J/(kg K)) of pure liquid methyl esters shown in Tables A1 and A2 are estimated based on the following general formula, valid in the temperature range 300 K $\leq T \leq$ min(700 K, $T_{\rm cr}$) [6, 41]:

$$c_l = \left(a_{pl} + b_{pl}T + c_{pl}T^2\right) \times 10^3 \ \ {\rm J/(kg\,K)}, \tag{39}$$

where the values of coefficients are given in Table A5 [6]. As in the case of Table A4, the coefficients for C18:3 M have been obtained via the linear extrapolation of the values of the coefficients for C18:1 M and C18:2 M.

Coeff.	C12:0 M – C24:0 M	C16:1 M – C24:1 M	C18:2 M	C18:3 M
a_{pl}	1.816	1.915	2.018	2.115
b_{pl}	-1.462×10^{-3}	-2.163×10^{-3}	-2.878×10^{-3}	-3.580×10^{-3}
c_{pl}	7.51×10^{-6}	8.29×10^{-6}	9.09×10^{-6}	9.92×10^{-6}

Table A5

Liquid diffusion coefficient

In our previous papers [8, 9, 15] it was suggested that the diffusion coefficient of component j relative to all other components can be estimated based on the simplified versions of the Sanchez and Clifton formula [38]:

$$D_{jm} = X_j D^0_{mj} + X_m D^0_{jm}, \tag{40}$$

where $_m$ refers to the mixture of all other components, D^0_{jm} and D^0_{mj} are diffusivities of dilute solute j in solvent m, and dilute solute m in solvent j

respectively, both are in m^2/s. Note that there are typos in the corresponding expressions for D_{jm} given in [8, 9].

At the same time it was shown in [42, 43] that a more accurate approximation for D_{jm} is given by the formula:

$$D_{jm} = (D^0_{mj})^{X_j}(D^0_{jm})^{X_m}. \tag{41}$$

(The authors are grateful to P. Kelley for drawing our attention to [42, 43].) In our case, the difference between Eqs. (40) and (41) is not important as the simplified model, based on the assumption that $D^0_{mj} = D^0_{jm}$, is used in our analysis (see below).

As in [8, 9], from amongst various approximations for D^0_{jm} and D^0_{mj} the Wilke-Chang approximation was chosen. This is given by the following formula [44]:

$$D^0_{AB} = \frac{7.4 \times 10^{-15}\sqrt{\varphi M_B}T}{\mu_B V_A^{0.6}}, \tag{42}$$

where M_B is the molar mass of solvent B, kg/kmol, T is the temperature in K, μ_B is the dynamic viscosity of solvent B (in kg $m^{-1}s^{-1}$), V_A is the molar volume of solute A at its normal boiling temperature, cm^3/mol (this can be recalculated from density if required, taking into account the molar mass of the substance), φ is the associated parameter of solvent B (following the recommendation by [44] it is assumed equal to 1).

This model is further simplified, assuming that D_{jm} is the same for all species and estimated as

$$D_{jm} \equiv D_l = \frac{7.4 \times 10^{-15}\sqrt{\overline{M}_v}T}{\mu_l V_v^{0.6}}, \tag{43}$$

where $\overline{M}_v$ is the average molar mass defined as

$$\overline{M}_v = \left[\sum_{i=1}^{i=N}(Y_i/M_i)\right]^{-1}, \tag{44}$$

mass fractions Y_i are linked with the molar fractions X_i by the following formula

$$Y_i = \frac{X_i M_i}{\sum_i M_i X_i}, \tag{45}$$

the summation is performed over all pure methyl esters in biofuels, N is the total number of pure methyl esters, V_v is defined as

$$V_v = (\sigma_v/1.18)^3\,, \tag{46}$$

where σ_v is the Lennard-Jones length (in Å). For individual components this length could be estimated based on the following formula [45]:

$$\sigma_v^3 = 0.17791 + 11.779\left(\frac{T_c}{p_c}\right) - 0.049029\left(\frac{T_c}{p_c}\right)^2, \tag{47}$$

where the critical temperatures T_c and pressure p_c are in K and bar respectively.

When estimating D_l for realistic biodiesel fuels shown in Table A1, these fuels could be approximated by the dominant components: C16:0 M for PME, C18:2 M for HME1, C18:2 M for HME2, C18:1 M for RME, C18:2 M for SME.

An alternative approach to the estimation of σ_v is based on the following formula [46]:

$$\sigma_v = 1.468\, M^{0.297}, \tag{48}$$

where M is the molar mass (in kg/kmole), and σ_v is in Å.

We found that Expression (48), with M identified as the mixture molar mass, is more convenient for calculations of σ_v, compared with Expression (47). Using Expression (48), the following values have been obtained: $\sigma_v =$ 7.86 Å for PME, $\sigma_v = 7.93$ Å for HME1, HME2 and SME, $\sigma_v = 8.05$ Å for RME. The above values of σ_v for SME and RME appeared to be close to the corresponding experimentally observed values reported in [47].

Alternative approaches to the estimation of σ_v are discussed in [40, 46, 48, 49]. These are not used in our analysis.

Saturated vapour pressure

The saturated vapour pressure (in Pa) of pure liquid methyl esters shown in Tables A1 and A2 can be estimated based on the following general formula, valid in the temperature range 260 K $\leq T \leq$ 610 K [50]:

$$p_v = 10^3 a_{\mathrm{CN},\,0}\left[a_{uc}(\mathrm{DB}+1) + b_{uc} + \frac{c_{uc}}{\mathrm{DB}+1}\right]\exp\left(a_{\mathrm{CN},\,1}\, n_{\mathrm{acid}}\right), \tag{49}$$

where

$$a_{\mathrm{CN},\,0} = 1.908\,\exp\left[0.01715\,T\right],$$

$$a_{\mathrm{CN},1} = -5.656 + 0.02649\,T - 4.5417 \times 10^{-5}\,T^2 + 2.6571 \times 10^{-8} T^3,$$

for DB = 0 or $T > 323$ K: $a_{uc} = c_{uc} = 0$, $b_{uc} = 1$, otherwise:

$$a_{uc} = 5.05 - 3.06 \times 10^{-2}\,T + 4.62 \times 10^{-5}\,T^2,$$

$$b_{uc} = -9.93 + 3.39 \times 10^{-2}\,T, \quad c_{uc} = 9.62 - 2.97 \times 10^{-2}\,T.$$

Vapour density is calculated from the ideal gas law as:

$$\rho_v = \frac{p_v M}{R_u T}, \tag{50}$$

where $R_u = 8.315$ kJ/(kmol K) is the universal gas constant.

Vapour diffusion coefficients

The formulae for binary diffusion coefficients of five dilute gaseous methyl esters in air, valid in the temperature range 300 K $\leq T \leq \min(T_{\mathrm{cr}}, 750$ K) and pressure equal to 1 bar are presented in Table A6 [31]:

Methyl ester	Binary diffusion coefficient of diluted methyl esters in air
C16:0 M	$D_v = 2.048241 \times 10^{-10}\,T^{1.75}$
C18:0 M	$D_v = 1.935023 \times 10^{-10}\,T^{1.75}$
C18:1 M	$D_v = 1.946548 \times 10^{-10}\,T^{1.75}$
C18:2 M	$D_v = 1.958266 \times 10^{-10}\,T^{1.75}$
C18:3 M	$D_v = 1.970184 \times 10^{-10}\,T^{1.75}$

Table A6

As follows from Table A6, the values of all diffusion coefficients are rather close. For our analysis we use only the average values of this coefficient for the mixtures of methyl esters. It is assumed that these values do not depend on the composition of this mixture and can be assumed equal to $D_v = 2 \times 10^{-10}\,T^{1.75}$. In the general case when p is not equal to 1 bar, this expression should be generalised to [44, 51]:

$$D_v = \frac{2 \times 10^{-10}\,T^{1.75}}{p}, \tag{51}$$

where p is pressure in bars. Expression (51) is used in our analysis.

Vapour heat capacity

Using data provided in [52], the following approximation for the vapour heat capacities of the components of biodiesel fuels in the range of temperatures $300 \leq T \leq 1200$ K is derived:

$$c_{pv} = a_{cpv}\tilde{T}^5 + b_{cpv}\tilde{T}^4 + c_{cpv}\tilde{T}^3 + d_{cpv}\tilde{T}^2 + e_{cpv}\tilde{T} + f_{cpv}, \qquad (52)$$

where $\tilde{T} = T/300$. The values of the coefficients for the components are given in Table A7.

Comp.	a_{cpv}	b_{cpv}	c_{cpv}	d_{cpv}	e_{cpv}	f_{cpv}
C12:0 M	0.027532	-1.509613	32.489208	-348.51699	1937.2422	-196.0638
C14:0 M	0.028031	-1.537655	33.11172	-355.3911	1975.95	-217.793
C16:0 M	0.02847	-1.562807	33.666284	2866.545	2008.022573	-236.281242
C17:0 M	-32.23395	359.06409	-1525.7052	2866.545	-1140.51	913.075
C18:0 M	0.029073	-1.592711	34.24248	-366.8571	2035.689	-252.356
C20:0 M	-33.507964	372.266358	-1578.271181	2963.634219	-1205.392857	929.231426
C22:0 M	-35.404232	392.035853	-1657.479888	3114.46656	-1334.93298	972.12171
C24:0 M	-38.172408	420.952853	-1773.590013	3337.37856	-1536.64767	1041.9097
C16:1 M	0.028355	-1.548214	33.141987	-353.10969	1946.7159	-194.6743
C18:1 M	0.028632	-1.565423	33.556761	-358.027218	1976.32596	-210.68717
C20:1 M	-37.732982	415.113425	-1742.582079	3261.99987	-1489.90392	1034.4857
C22:1 M	-43.35771	473.480486	-1975.083156	3702.98628	-1869.74505	1162.5471
C24:1 M	-48.982436	531.847544	-2207.584225	4143.97269	-2249.586144	1290.60857
C18:2 M	0.028537	-1.552823	33.097465	-350.761281	1921.716581	-176.117655
C18:3 M	0.02823	-1.531367	32.505573	-342.625176	1864.607187	-140.492938
Other	0.028632	-1.565423	33.556761	-358.027218	1976.32596	-210.68717

Table A7

For the component identified as 'Other' the parameters for C18:1 M have been used. These provided the required average values for c_{pv} calculated using the remaining components.

Gas viscosity and thermal conductivity

We assume that fuel vapour is sufficiently diluted to allow us to consider both these transport coefficients for the mixture to be equal to that for air.

In contrast to our previous papers [8, 9], both these properties have been obtained based on the approximations of reported experimental data [53]. In the case of dynamic viscosity, the theoretical formula used in [8, 9] (see Eq. D.6-2 on page 861 of [44]) gave an almost perfect approximation of the experimental data and it was used in our analysis. In the case of thermal conductivity, however, the theoretical formula used in [8, 9] (see Eq. D.6-3 on page 861 of [44]) underpredicted the experimental data given in [53] by up to about 10% (especially at high temperatures). In our analysis the following approximation of data for thermal conductivity of air given in [53], valid in the range of temperatures from 250 K to 1200 K, was used

$$k_{\mathrm{air}} = -0.00189\,\tilde{T}^2 + 0.0252\,\tilde{T} + 0.0036, \tag{53}$$

where $\tilde{T} = T/300$.

Appendix 3

Transport and thermodynamic properties of biodiesel fuels

Average values

Data presented in Appendix 2 allow us to calculate average values of liquid density, specific heat capacity, dynamic viscosity and thermal conductivity using the following formulae [8, 9]:

$$\overline{\rho}_l = \left[\sum_{i=1}^{i=N} \left(Y_i/\rho_{li}\right)\right]^{-1}, \tag{54}$$

$$\overline{c}_l = \sum_{i=1}^{i=N} \left(Y_i c_{li}\right), \tag{55}$$

$$\ln \overline{\mu}_l = \sum_{i=1}^{i=N} X_i \ln \mu_{li}, \tag{56}$$

$$\overline{k}_l = \left(\sum_{i=1}^{i=N} Y_i k_{li}^2\right)^{-1/2}, \tag{57}$$

where the subscripts $_{li}$ refer to the corresponding liquid components (Eqs. (56)-(57) are approximate).

The values of the average latent heat of evaporation and saturated vapour pressure are estimated as in [15] based on the equations:

$$\overline{L} = \sum_{i=1}^{i=N} \epsilon_i L_i, \tag{58}$$

$$\overline{p}_v = \sum_{i=1}^{i=N} X_i p_{vi}. \tag{59}$$

Comparison of the values

In this section, the values of parameters predicted by Eqs. (54)-(59) are compared with the values reported by other authors (measured or calculated) where possible.

Liquid density. The values of liquid density (estimated [54] and calculated Eqs. (54) and (30) for Palm Methyl Ester (PME), Rapeseed oil Methyl Ester (RME), and Soy oil Methyl Ester (SME) are compared in Table A8. We have presented the values of densities only for the cases for which results were reported in [54].

Temperature	**PME**	**RME**	**SME**
	Measured /Calculated	Measured/Calculated	Measured/Calculated
293.15 K	-	886.4/878.823	891.4/882.303
298.15 K	876.0/867.303	-	-
313.15 K	866.4/856.382	871.4/864.634	876.4/867.9
333.15 K	849.3/843.62	864.3/850.445	869.4/853.497
353.15 K	841.3/827.260	849.3/ 836.256	856.3/839.094
360.15 K	834.3/822.161	841.3/831.290	846.3/834.053

Table A8

As one can see from Table A8, the agreement between the values of density predicted by both approaches is reasonably good. In our calculations the gradients of density inside droplets are ignored. The average density is calculated based on the average temperature and composition inside the droplets as was done in [8, 9].

Liquid viscosity. The values of liquid dynamic viscosities (in kg/(m s)) reported by [54] and calculated from Eqs. (56), (31), (32) for Palm Methyl Ester (PME), Rapeseed oil Methyl Ester (RME), and Soybean oil Methyl Ester (SME) are compared in Table A9. We have presented the values of dynamic viscosities only for the cases for which results were reported in [54].

Temperature	**PME**	**RME**	**SME**
	Measured /Calculated	Measured/Calculated	Measured/Calculated
293.15 K	-	0.006777/0.00583394	0.005853/0.00511201
298.15 K	0.006041/0.00548836	-	-
313.15 K	0.004256/0.00388956	0.004212/0.0038166	0.003785/0.00342128
333.15 K	0.002954/0.00257629	0.003052/0.00262691	0.002793/0.00238586
353.15 K	0.002158/0.00178582	0.002251/0.0018860	0.002099/0.00173252
373.15 K	0.001654/0.00158557	0.001646/0.0016940	0.001537/0.001561884

Table A9

As one can see from Table A9, the agreement between the values of dynamic viscosity predicted by both approaches is reasonably good. They differ by not more than 17% which is perfectly acceptable for our analysis remembering that the results are rather weak functions of viscosity in most cases. This is consistent with the results of measurements of biodiesel viscosities reported by various authors. For example, the values of viscosities for two different RMEs at temperature 293.15 K measured by [55] turned out to be 6.09×10^{-3} kg/(m s) and 6.24×10^{-3} kg/(m s). These values are more that 8% smaller than those measured by [54]. As in the case of density, in our calculations the gradients of dynamic viscosity inside droplets are ignored. The average dynamic viscosity is calculated based on the average temperature and composition inside the droplets as was done in [8, 9] for Diesel and gasoline fuels.

Liquid thermal conductivity and latent heat of evaporation. The values of liquid thermal conductivity (estimated [54]; calculated Eqs. (57) and (36), modified Latini method) (in W/(m K)) of Palm Methyl Ester (PME), Rapeseed oil Methyl Ester (RME), and Soybean oil Methyl Ester (SME) are compared in Table A10. We have presented the values of dynamic viscosities only for

the cases for which results were reported in [54]. The results for temperatures below 300 K, not relevant for most automotive applications, are not included in this table.

Temp.	**PME**	**RME**	**SME**
	Estimated/Calculated	Estimated/Calculated	Estimated/Calculated
300 K	0.16999/0.1695	0.17696/0.16423	0.17887/0.167862
350 K	0.16158/0.158077	0.1686/0.15349	0.17031/0.15672
400 K	0.15282/0.14711	0.15991/0.143202	0.16139/0.146016
450 K	0.14361/0.136234	0.15083/0.13306	0.15204/0.135435
500 K	0.13384/0.1251531	0.14125/0.12280	0.14216/0.124685
550 K	0.12333/0.1181	0.13104/0.11415	0.13159/0.116403
600 K	0.1118/0.118093	0.11997/0.113173	0.12007/0.116387

Table A10

As one can see from Table A10, the agreement between the values of thermal conductivity predicted by both approaches is reasonably good. They differ by not more than 14%. The measurements of thermal conductivity of SME and RME reported by [56] predicted values 0.154±0.002 W/(m K) and 0.149±0.001 W/(m K) respectively at room temperature. These values are reasonably close to those presented in Table A10. The values predicted by the original Latini method (Eq. (33)) would lead to values of thermal conductivity about 50% less than those reported in [54]. Until we are able to understand the root of this deviation, the modified Latini method will be used to estimate the liquid thermal conductivity. As in the case of density and dynamic viscosity, in our calculations the gradients of thermal conductivity inside droplets are ignored. The average thermal conductivity is calculated based on the average temperature and composition inside the droplets as was done in [8, 9].

The values of the molar latent heat of evaporation of SME in the temperature range from below 300 K to almost 800 K are presented in [57] in graphical form. This heat was shown to be lower than that of Diesel fuel at low temperatures but higher than that of Diesel fuel at high temperatures [58].

Liquid heat capacity. The calculated values of the molar heat capacity of SME in the temperature range from 300 K to 600 K are presented in [57] in graphical form. It was shown to increase almost linearly with temperature. Similar results but for canola and coconut biodiesel fuels and in a narrower temperature range (283 – 328 K) were reported in [50].

Saturated vapour pressure. The following approximation for the saturated vapour pressure of SME (in bars) was suggested in [57], based on data provided by [59]:

$$\log_{10} p_v = 76.08 - 8143\, T^{-1} - 23.01\, \log_{10}(T) + 6.0000 \times 10^{-5}\, T + 3.2 \times 10^{-6}\, T^2. \tag{60}$$

The temperature range applicability of this equation is (300-353 K).

Similar results but for canola and coconut biodiesel fuels and in a graphical form in the temperature range from about 323 K to 473 K, using experimental data from [60], were reported in [50]. In general, the saturated vapour pressures for biodiesel fuel were shown to be much lower than those for Diesel fuel [58].

References

[1] Lapuerta M, Armas O, Rodrigues-Fernandez J. Effect of biodiesel fuels on diesel engine emissions. Progress in Energy and Combustion Science 2008;34:198-223.

[2] Hoekman SK, Broch A, Robbins C, Ceniceros E, Natarajan M. Review of biodiesel composition, properties, and specifications. Renewable and Sustainable Energy Reviews 2012;16:143169.

[3] van Gerpen J. Biodiesel processing and production. Fuel Processing Technology 2005;86:1097-107.

[4] Knothe G. Biodiesel and renewable diesel: a comparison. Progress in Energy and Combustion Science 2010;36:364-73.

[5] Grabar IG, Kolodnytska RV, Semenov VG. Biofuel based on oil for diesel engines. Zhytomyr: ZDTU; 2011 (In Ukrainian).

[6] Hallett WHL, Legault NV. Modelling biodiesel droplet evaporation using continuous thermodynamics. Fuel 2011;90:1221-8.

[7] Saha K, Abu-Ramadan E, Li H. Multicomponent evaporation model for pure and blended biodiesel droplets in a high temperature convective environment. Applied Energy 93;2012:71-79.

[8] Sazhin SS, Elwardany A, Krutitskii PA, Castanet G, Lemoine F, Sazhina EM, Heikal MR. A simplified model for bi-component droplet heating and evaporation. Int. J of Heat and Mass Transfer 2010;53:4495-505.

[9] Sazhin SS, Elwardany A, Krutitskii PA, Deprédurand V, Castanet G, Lemoine F, Sazhina EM, Heikal MR. Multi-component droplet heating and evaporation: numerical simulation versus experimental data, Int. J of Thermal Science 2011;50:1164-80.

[10] Carslaw HS, Jaeger JC. Conduction of Heat in Solids. Oxford: Clarendon Press, 1986.

[11] Kartashov EM. Analytical Methods in Heat Transfer Theory in Solids. Moscow: Vysshaya Shkola; 2001 (in Russian).

[12] Abramzon B, Sirignano WA. Droplet vaporization model for spray combustion calculations, Int J Heat and Mass Transfer 1989;32:1605-18.

[13] Sazhin SS, Krutitskii PA, Abdelghaffar WA, Mikhalovsky SV, Meikle ST, Heikal MR. Transient heating of diesel fuel droplets, Int J Heat Mass Transfer 2004;47:3327-40.

[14] Sazhin SS, Krutitskii PA. A conduction model for transient heating of fuel droplets. In Begehre HGW, Gilbert RP, Wong MW, editors. Progress in Analysis Vol. II. Proceedings of the 3rd International ISAAC (International Society for Analysis, Applications and Computations) Congress (August 20 - 25, 2001, Berlin), Singapore: World Scientific; 2003, pp. 1231-9.

[15] Sazhin SS, Elwardany A, Sazhina EM, Heikal MR. A quasi-discrete model for heating and evaporation of complex multicomponent hydrocarbon fuel droplets. Int. J. of Heat and Mass Transfer 2011;54:4325-32.

[16] Elwardany AE, Sazhin SS. (2012) A quasi-discrete model for droplet heating and evaporation: application to Diesel and gasoline fuels. Fuel 2012;97:685-94.

[17] Elwardany AE, Sazhin SS, Farooq A. Modelling of heating and evaporation of gasoline fuel droplets: a comparative analysis of approximations, Fuel 2013 (in press).

[18] Sazhin SS. Advanced models of fuel droplet heating and evaporation, Prog. in Energy Combustion Sci. 2006;32:162-214.

[19] Elwardany AE, Gusev IG, Castanet G, Lemoine F, Sazhin SS. Mono- and multi-component droplet cooling/heating and evaporation: comparative analysis of numerical models. Atomization and Sprays 2011;21(11):907-31.

[20] Maqua C, Castanet G, Lemoine F. Bi-component droplet evaporation: temperature measurements and modelling. Fuel 2008;87:2932-42.

[21] Sazhin SS, Abdelghaffar WA, Krutitskii PA, Sazhina EM, Heikal MR. New approaches to numerical modelling of droplet transient heating and evaporation. Int J Heat Mass Transfer 2005;48:4215-28.

[22] Atkins P, de Paula J. Atkins' Physical Chemistry, Seventh Edition, Oxford University Press; 2002.

[23] Ejim CE, Fleck BA, Amirfazli A. Analytical study for atomization of biodiesels and their blends in a typical injector: Surface tension and viscosity effects. Fuel 2007;86:1534-44.

[24] Kolodnytska RV. Analytical study for atomization of hemp oil biodiesel. Visnik Shydno-Ukrainskogo Natyonalnogo Universitetu imeni Volodymira Dalya 2010;6(148):41-46. (In Ukrainian).

[25] Chen PC, Wang WC, Roberts WL, Fang T. Spray and atomization of diesel fuel and its alternatives from a single-hole injector using a common rail fuel injection system. Fuel 2013;103:850-61.

[26] Som S, Longman DE, Ramirez AI, Aggarwal SK. A comparison of injector flow and spray characteristics of biodiesel with petrodiesel. Fuel 2010;89:4014-24.

[27] Schonborn A, Ladommatos N, Williams J, Allan R, Rogerson J. The influence of molecular structure of fatty acid monoalkyl esters on diesel combustion. Combustion and Flame 2000;156:1396-412.

[28] Emberger P, Thuneke K, Haas R, Remmele E. Examination of hemp oil with regard to its suitability as fuel for engines adapted to pure plant oil use. (http://www.nova-institut.de) 2007.

[29] Ramirez-Verduzco LF, Rodriguez-Rodriguez JE, Jaramillo-Jacob AE. Predicting the cetane number, kinematic viscosity, density and higher heating value of biodiesel from its fatty acid methyl ester composition. Fuel 2012;91:102-11.

[30] Lapuerta M, Rodriguez-Fernandez J, Oliva F. Determination of the enthalpy of formation of methyl and ethyl esters of fatty acids. Chemistry and Physics of Lipids 2010;163:172-181.

[31] An H, Yang WM, Maghbouli A, Chou SK, Chua KJ. Detailed Physical properties prediction of pure methyl esters for biodiesel combustion modeling. Appl Energy. 2013;102:647-56.

[32] Yaws CL, Thermophysical Properties of Chemicals and Hydrocarbons. William Andrew Inc. 2008.

[33] Lapuerta M, Rodriguez-Fernandez J, Armas O. Correlation for the estimation of the density of fatty acid ester fuels and its implications. A proposed Biodiesel Cetane Index. Chemistry and Physics of Lipids 2010;163:720-7.

[34] Krisnangkura K, Yimsuwan T, Pairinta R. An empirical approach in predicting biodiesel viscosity at various temperatures. Fuel 2006;85:107-13.

[35] Yuan W, Hansen AC, Zhang Q. 2003. Predicting the Physical Properties of Biodiesel for Combustion Modeling, Transactions of the ASAE 2003;46:1487-93.

[36] Reid RC, Prausnitz JM, Poling BE. The Properties of Gases and Liquids. Fourth edition. McGraw-Hill, Inc. 1987.

[37] Latini G, Grifoni RC, Passerini G. Transport Properties of Organic Liquids. WIT press, Southampton, UK, 2006.

[38] Poling BE, Prausnitz JM, O'Connell J. The Properties of Gases and Liquids. New York: McGraw-Hill; 2000.

[39] Anand, A, Sharma, RP, Mehta, PS. A comprehensive approach for estimating thermo-physical properties of biodiesel fuels. App. Therm. Eng. 2011;31:235-42.

[40] Dievart P, Won SH, Dooley S, Dryer FL, Ju Y. A kinetic model for methyl decanoate combustion. Combustion and Flame 2012;159:1793-805.

[41] Hallett WLH, Clark NA. A model for the evaporation of biomass pyrolisis oil droplets. Fuel 2006;85:532-44.

[42] Vignes A. Diffusion in binary solutions. Industrial & Engineering Chemistry Fundamentals 1966;5(2):189-99.

[43] Kneer R. Grundlegende Untersuchungen zur Sprühstrahlausbreitung in hochbelasteten Brennräumen: Tropfenverdunstung und Sprühstrahlcharakterisierung. Dissertation Doktors der Ingenieurwissenschaften, Karlsruhe 1993.

[44] Bird RB, Stewart EW, Lightfoot EN. Transport Phenomena, Second Edition. New York, Chichester: Wiley & Sons; 2002.

[45] Hirschfelder JO, Curtiss CF, Bird RB. Molecular Theory of Gases and Liquids. 4th ed. New York: Wiley; 1967.

[46] Dooley S, Uddi M, Won SH, Dryer FL, Ju Y. Methyl butanoate inhibition of n-heptane diffusion flames through an evaluation of transport and chemical kinetics, Combustion and Flame 2012;159:1371-84.

[47] Magalhães AL, Da Silva FA, Silva CM. New models for tracer diffusion coefficients of hard sphere and real systems: application to gases, liquids and supercritical fluids, J. of Supercritical Fluids 2011;55:898-923.

[48] Perdomo FA, Gil-Villegas A. Molecular thermodynamics of biodiesel fuel compounds, Fluid Phase Equilibria 2010;293:182-9.

[49] Wang YL, Feng Q, Egolfopoulos FN, Tsotsis Th.T. Studies of C4 and C10 methyl ester flames. Combustion and Flame 2011;158:1507-19.

[50] Diaz OC, Schoeggl F, Yarranton HW, Satyro MA, Lovestead TM, Bruno TJ. Modelling the vapour pressure of biodiesel fuels. World Academy of Science, Engineering and Technology (WASET) 2012;65:876-86.

[51] Abramzon B, Sazhin SS. Convective vaporization of fuel droplets with thermal radiation absorption. Fuel 2006;85:32-46.

[52] Osmont A, Catoire L, Gökalp, I. Thermochemistry of Methyl and Ethyl Esters from Vegetable Oils. Published online in Wiley InterScience, DOI 10.1002/kin.20264.

[53] Incropera FP, DeWitt DP. Fundamentals of Heat and Mass Transfer, Fifth Edition. New York, Chichester: Wiley & Sons; 2002.

[54] McCrady J, Hansen A, Lee CF. Physical property measurement of biodiesel fuels for low temperature combustion modelling. An ASABE Meeting Presentation. UILU 2006 -7020. Paper Number: 066146.

[55] Kerschbaum S, Rinke G. Measurement of the temperature dependent viscosity of biodiesel fuels. Fuel 2004;83:287-91.

[56] Machado FAL, Zanelato EB, Guimaraes AO, da Silva EC. Thermal properties of biodiesel and their corresponding precursor vegetable oils obtained by photopyroelectric methodology. Int J Thermophys 2012;33:1848-55. DOI 10. 1007/s10765-012-1245-6.

[57] Chakravarthy K, McFarlane J, Daw S, Ra Y, Reitz R, Griffin J. Physical properties of bio-Diesel and implications for use of bio-Diesel in Diesel engines. SAE 2007-01-4030.

[58] Vertes AA, Qureshi N, Blaschek HP, Yukawa H (Editors). Biomass to Biofuels: Strategies for Global Industries. John Wiley 2009.

[59] Yuan W, Hansen AC, Zhang Q. Predicting the Physical Properties of Biodiesel for Combustion Modeling, Transactions of the ASAE 2003;46:1487-93.

[60] Goodrum JW. Volatility and boiling points of biodiesel from vegetable oils and tallow. Biomass and Bioenergy 2002;22:205-11.

Figure captions

Fig. 1 The plots of PME droplet surface temperatures (T_s) and radii (R_d) versus time predicted by the multi-component (M) and single component (S) models. Gas temperature and pressure are assumed to be equal to 880 K and 30 bar respectively. The initial droplet radius is assumed to be equal to 12.66 μm. The droplet is assumed to be stationary. The analysis is based on the Effective Thermal Conductivity/Effective Diffusivity (ETC/ED) model.

Fig. 2 The plots of liquid surface mass fractions (Y_{lis}) of methyl palmitate (C16:0 M), methyl stearate (C18:0 M), methyl oleate (C18:1 M), methyl linoleate (C18:2 M) and methyl eicosenoate (C20:1 M) versus time for the same droplet as in Fig. 1.

Fig. 3 The plots of liquid mass fractions (Y_{li}) of methyl palmitate (C16:0 M) and methyl oleate (C18:1 M) versus normalised distance from the centre of the droplet R/R_d at three instants of time (0.3 ms, 1 ms and 2 ms) for the same droplet as in Figs. 1 and 2.

Fig. 4 The plots of temperature (T) versus normalised distance from the centre of the droplet R/R_d at five instants of time (0.02 ms, 0.3 ms, 0.5 ms, 1 ms and 2 ms) for the same droplet as in Figs. 1-3.

Fig. 5 The plots of HME1 droplet surface temperatures (T_s) and radii (R_d) versus time predicted by the multi-component (M) and single component (S) models. The gas and initial droplet parameters are the same is in Fig. 1. The analysis is based on the Effective Thermal Conductivity/Effective Diffusivity (ETC/ED) model.

Fig. 6 The plots of liquid surface mass fractions (Y_{lis}) of methyl palmitate (C16:0 M), methyl tetracosanoate (C24:0 M), methyl oleate (C18:1 M), methyl linoleate (C18:2 M) and methyl linolenate (C18:3 M) versus time for the same droplet as in Fig. 5.

Fig. 7 The plots of HME2 droplet surface temperatures (T_s) and radii (R_d) versus time predicted by the multi-component (M) and single component (S) models. The gas and initial droplet parameters are the same is in

Fig. 1. The analysis is based on the Effective Thermal Conductivity/Effective Diffusivity (ETC/ED) model.

Fig. 8 The plots of liquid surface mass fractions (Y_{lis}) of methyl palmitate (C16:0 M), methyl eicosanoate (C20:0 M), methyl oleate (C18:1 M), methyl linoleate (C18:2 M) and methyl linolenate (C18:3 M) versus time for the same droplet as in Fig. 7.

Fig. 9 The plots of RME droplet surface temperatures (T_s) and radii (R_d) versus time predicted by the multi-component (M) and single component (S) models. The gas and initial droplet parameters are the same is in Fig. 1. The analysis is based on the Effective Thermal Conductivity/Effective Diffusivity (ETC/ED) model.

Fig. 10 The plots of liquid surface mass fractions (Y_{lis}) of methyl palmitate (C16:0 M), methyl oleate (C18:1 M), methyl nervonate (C24:1 M), methyl linoleate (C18:2 M) and methyl linolenate (C18:3 M) versus time for the same droplet as in Fig. 9.

Fig. 11 The plots of SME droplet surface temperatures (T_s) and radii (R_d) versus time predicted by the multi-component (M) and single component (S) models. The gas and initial droplet parameters are the same is in Fig. 1. The analysis is based on the Effective Thermal Conductivity/Effective Diffusivity (ETC/ED) model.

Fig. 12 The plots of liquid surface mass fractions (Y_{lis}) of methyl palmitate (C16:0 M), methyl stearate (C18:0 M), methyl oleate (C18:1 M), methyl erucate (C22:1 M), methyl linoleate (C18:2 M) and methyl linolenate (C18:3 M) versus time for the same droplet as in Fig. 11.

Fig. 13 The plots of PME droplet surface temperatures (T_s) and radii (R_d) versus time predicted by the multi-component (M) and single component (S) models. Gas temperature and pressure are assumed to be equal to 880 K and 30 bar respectively. The initial droplet radius is assumed to be equal to 12.66 μm. The droplet is assumed to be moving with a constant velocity equal to 10 m/s. The analysis in both cases is based on the Effective Thermal Conductivity/Effective Diffusivity (ETC/ED) model and in the case of the multi-component model it is also based on the Infinite Thermal

Conductivity/Infinite Diffusivity (ITC/ID) model (IM).

Fig. A1 Schematic presentations of the structures of C18:0 M, C18:1 M and C18:2 M molecules.

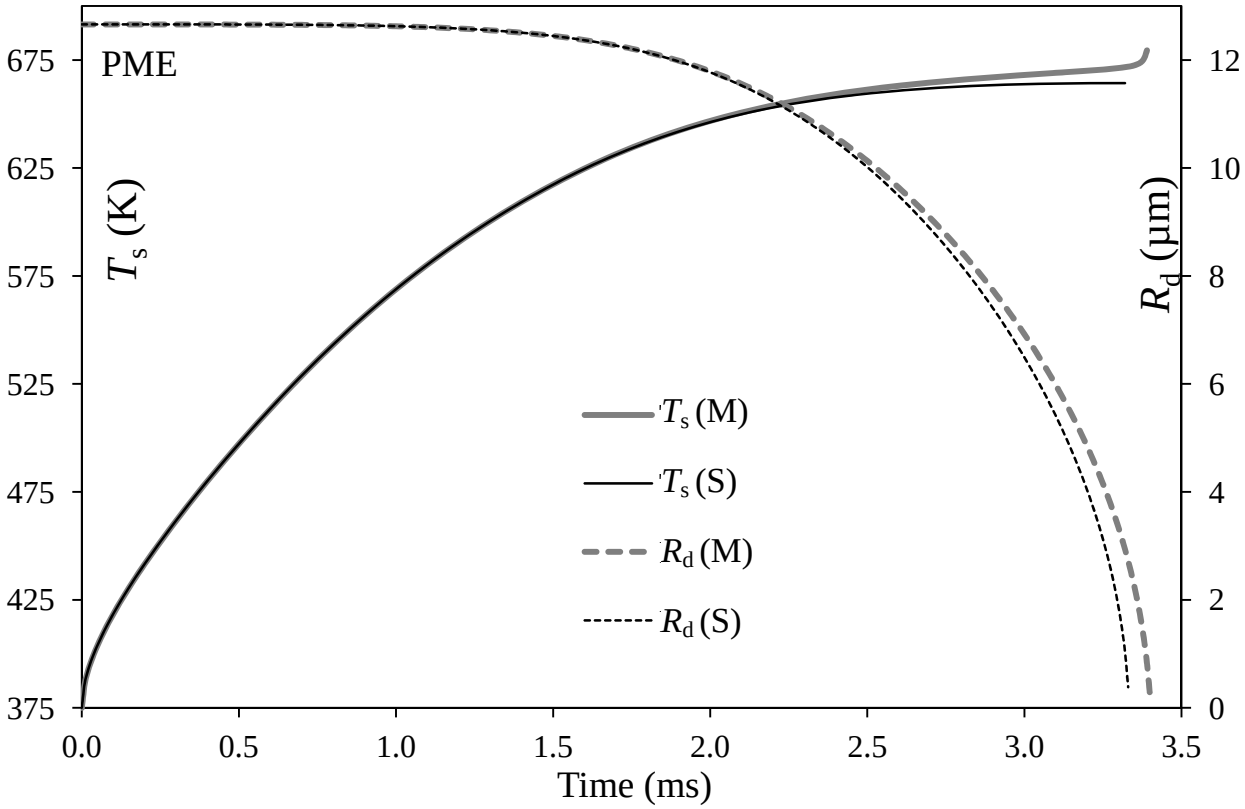
PME
T_s (K)
R_d (μm)
T_s (M)
T_s (S)
R_d (M)
R_d (S)
675
625
575
525
475
425
375
12
10
8
6
4
2
0
0.0
0.5
1.0
1.5
2.0
2.5
3.0
3.5
Time (ms)

Fig. 1

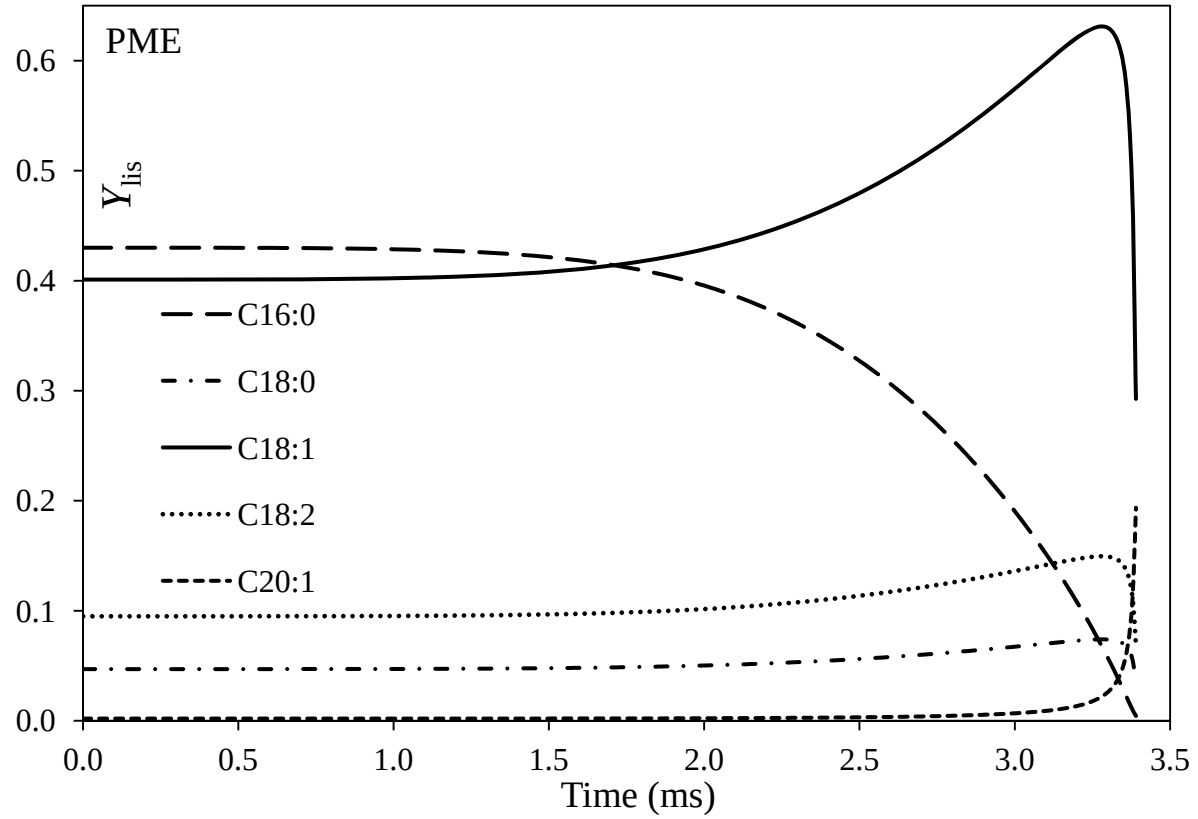
PME
Y_{lis}
C16:0
C18:0
C18:1
C18:2
C20:1
0.6
0.5
0.4
0.3
0.2
0.1
0.0
0.0
0.5
1.0
1.5
2.0
2.5
3.0
3.5
Time (ms)

Fig. 2

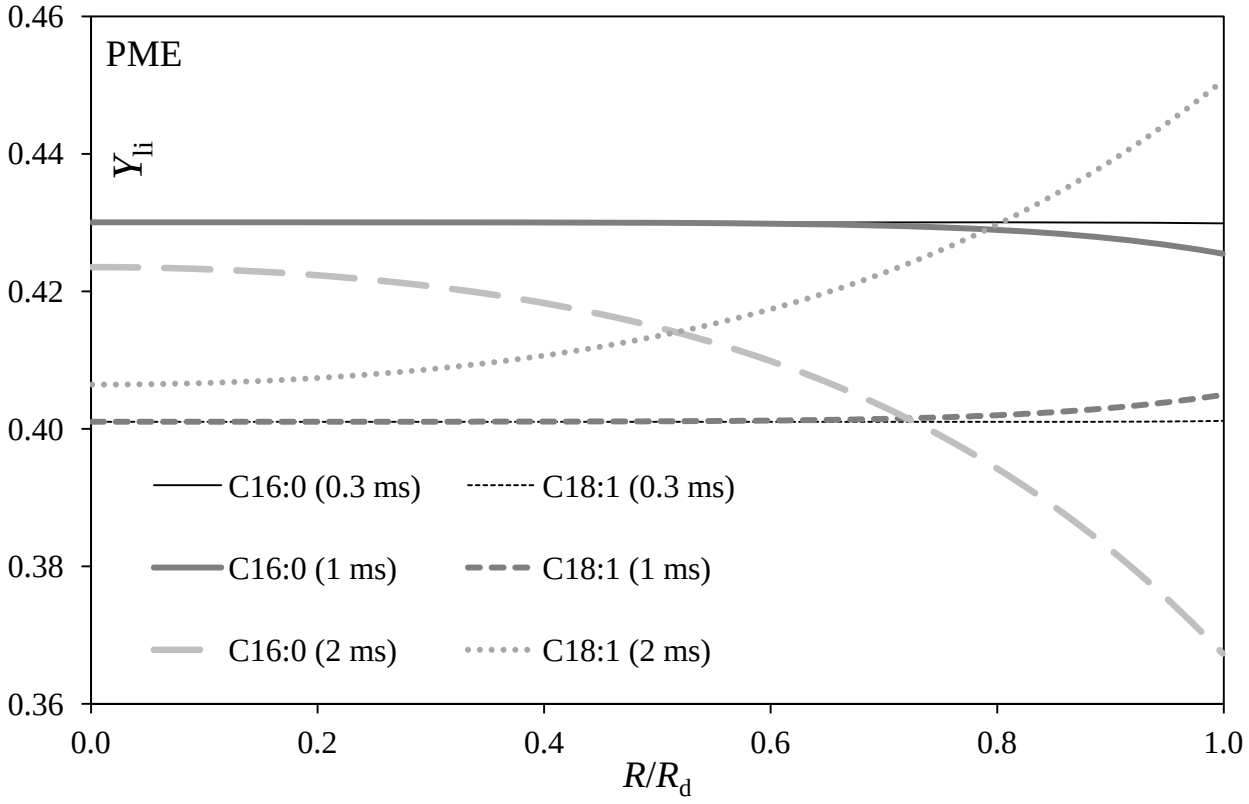
PME
Y_{li}
0.46
0.44
0.42
0.40
0.38
0.36
C16:0 (0.3 ms)
C18:1 (0.3 ms)
C16:0 (1 ms)
C18:1 (1 ms)
C16:0 (2 ms)
C18:1 (2 ms)
0.0
0.2
0.4
0.6
0.8
1.0
R/R_d

Fig. 3

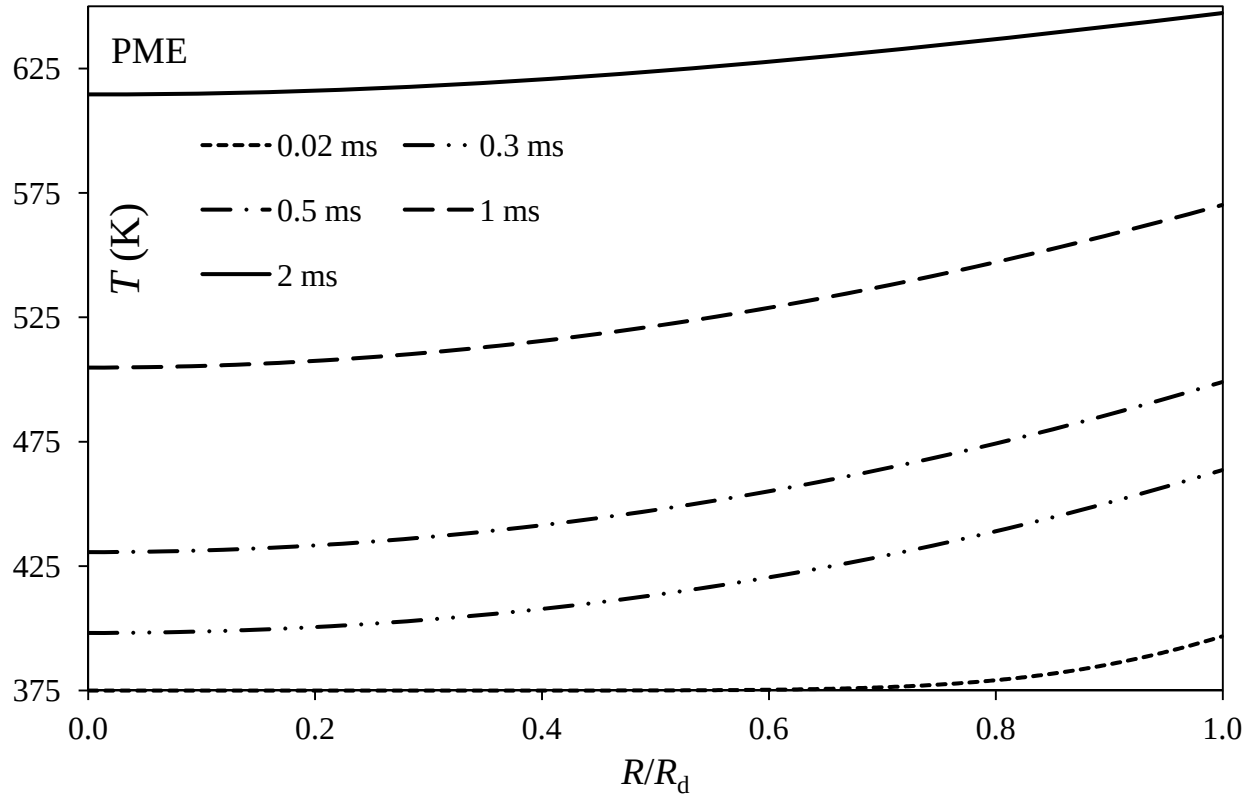
PME
T (K)
625
575
525
475
425
375
0.02 ms
0.3 ms
0.5 ms
1 ms
2 ms
0.0
0.2
0.4
0.6
0.8
1.0
R/R_d

Fig. 4

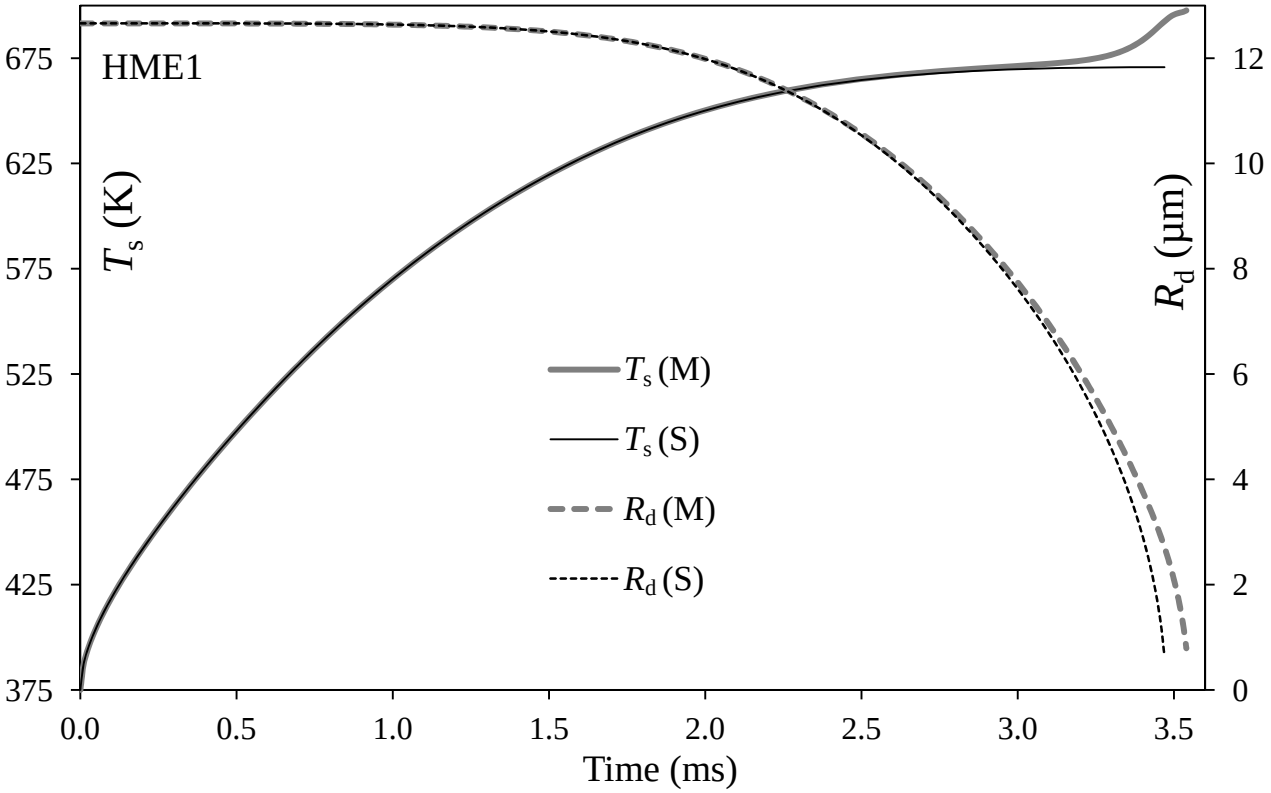
HME1
T_s (K)
R_d (μm)
T_s (M)
T_s (S)
R_d (M)
R_d (S)
675
625
575
525
475
425
375
12
10
8
6
4
2
0
0.0
0.5
1.0
1.5
2.0
2.5
3.0
3.5
Time (ms)

Fig. 5

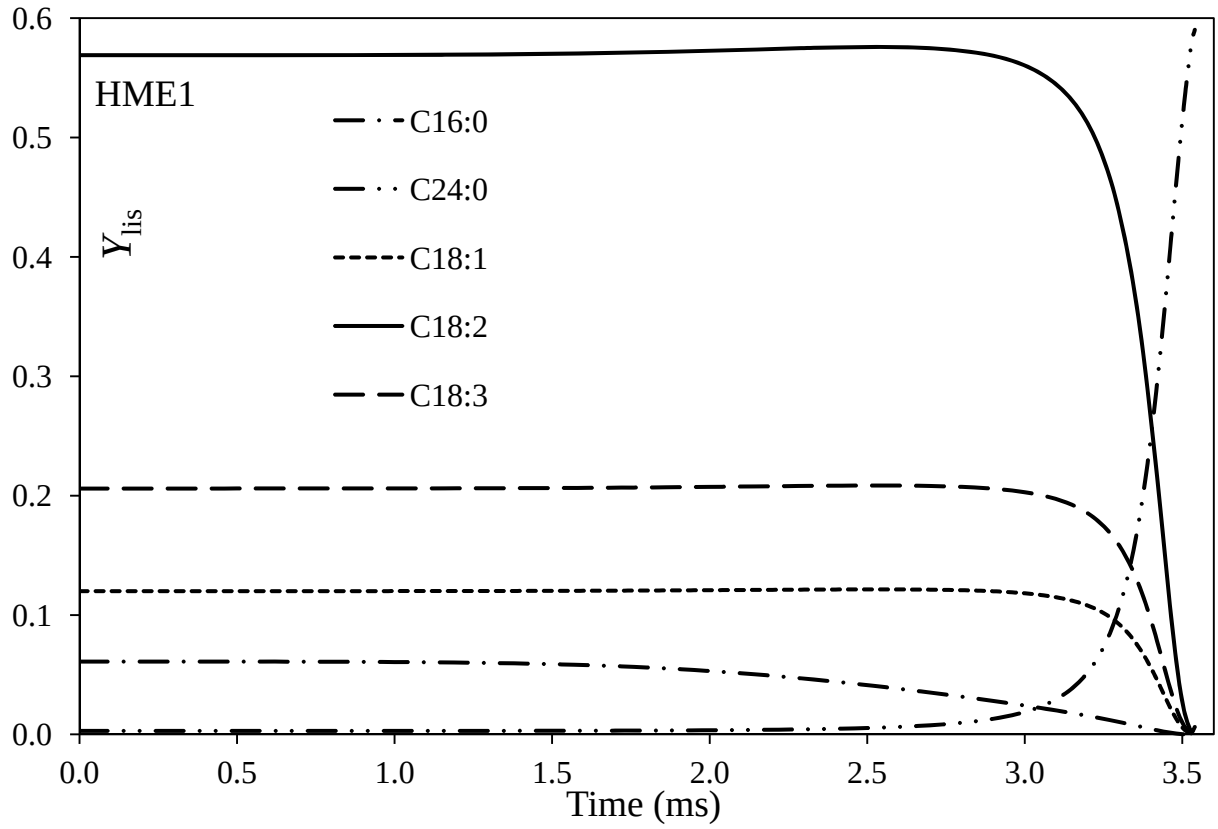
HME1
Y_{lis}
C16:0
C24:0
C18:1
C18:2
C18:3
0.6
0.5
0.4
0.3
0.2
0.1
0.0
0.0
0.5
1.0
1.5
2.0
2.5
3.0
3.5
Time (ms)

Fig. 6

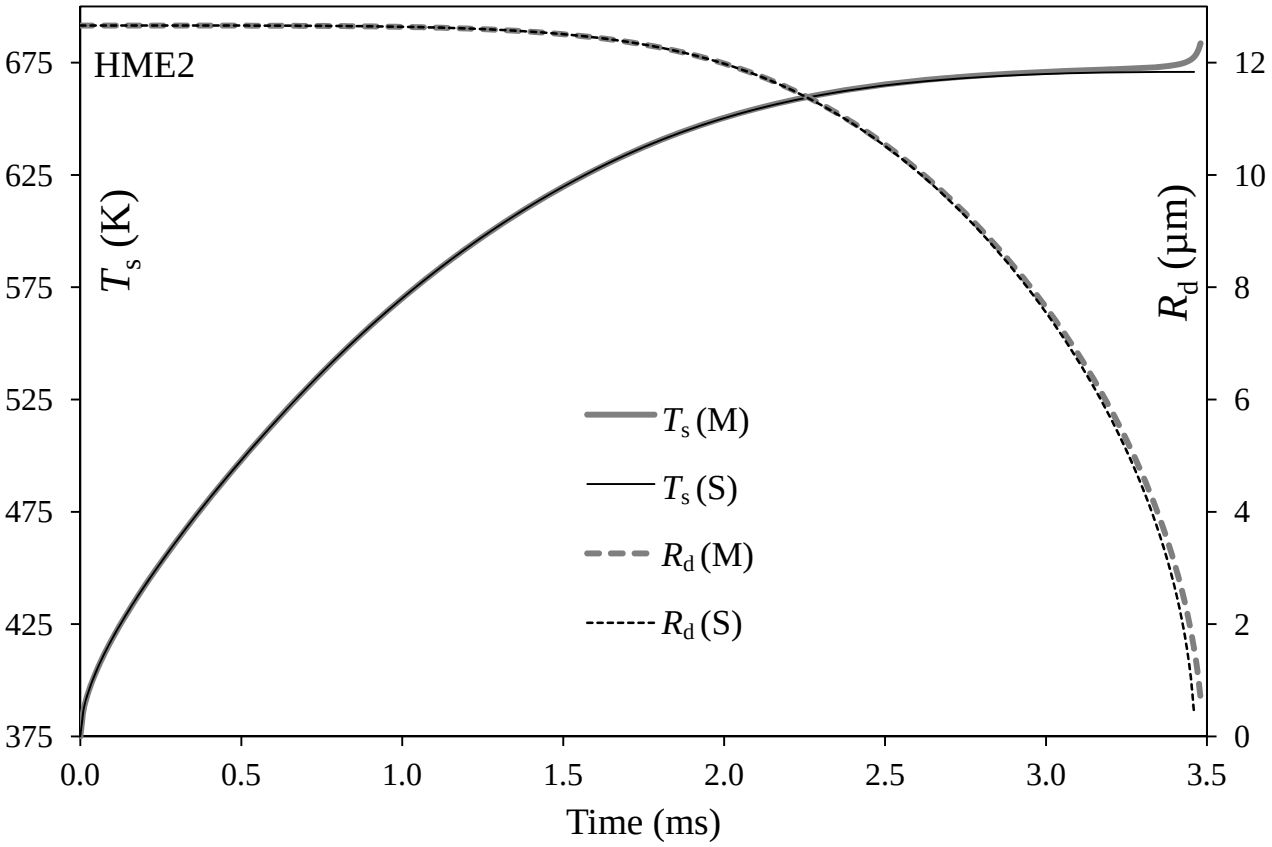
HME2
T_s (K)
R_d (μm)
T_s (M)
T_s (S)
R_d (M)
R_d (S)
675
625
575
525
475
425
375
12
10
8
6
4
2
0
0.0
0.5
1.0
1.5
2.0
2.5
3.0
3.5
Time (ms)

Fig. 7

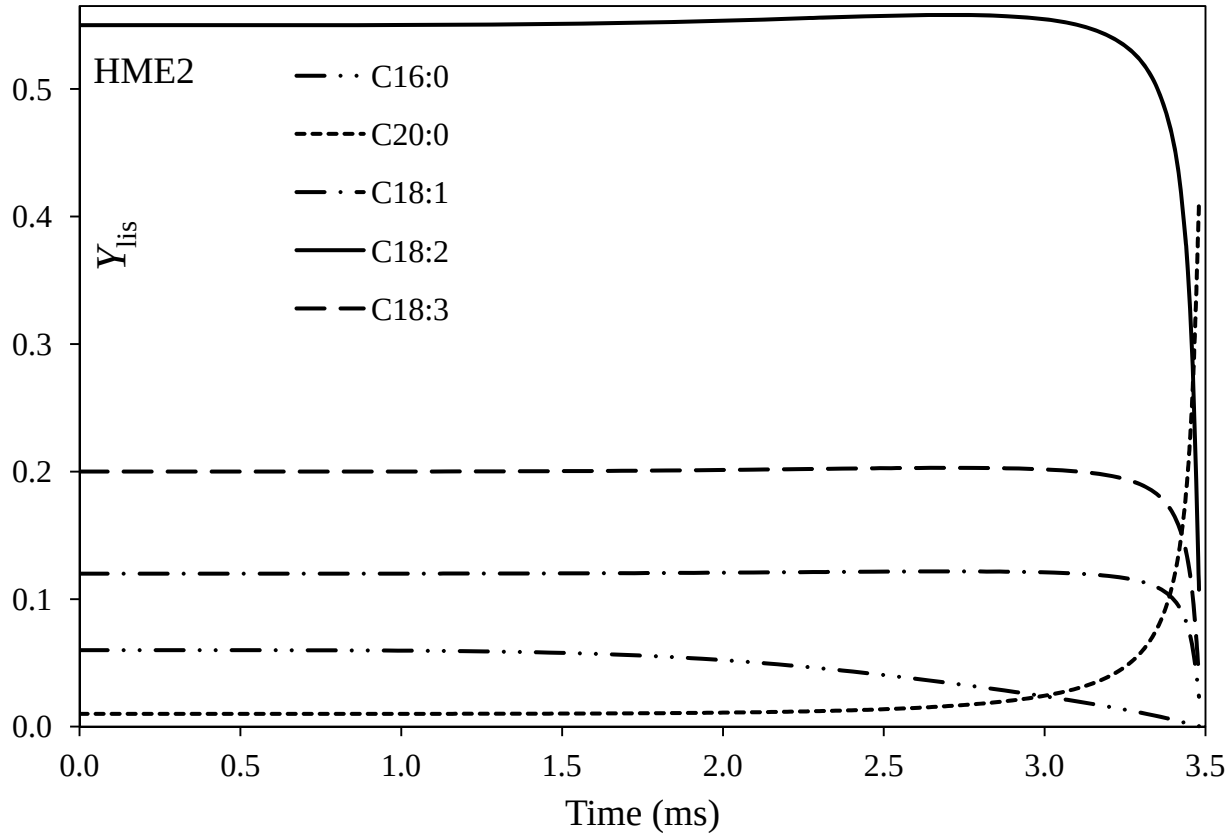
HME2
Y_{lis}
C16:0
C20:0
C18:1
C18:2
C18:3
0.5
0.4
0.3
0.2
0.1
0.0
0.0
0.5
1.0
1.5
2.0
2.5
3.0
3.5
Time (ms)

Fig. 8

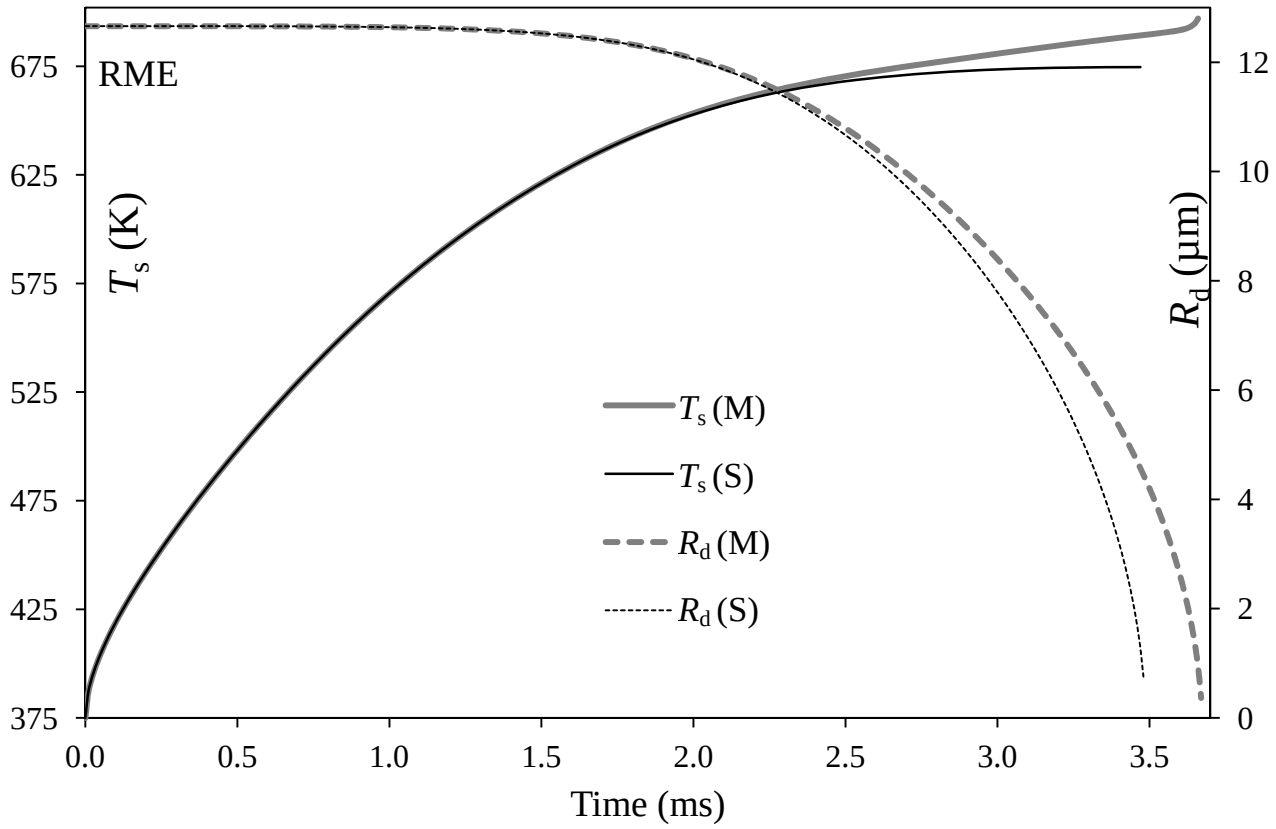
RME
T_s (K)
R_d (μm)
T_s (M)
T_s (S)
R_d (M)
R_d (S)
675
625
575
525
475
425
375
12
10
8
6
4
2
0
0.0
0.5
1.0
1.5
2.0
2.5
3.0
3.5
Time (ms)

Fig. 9

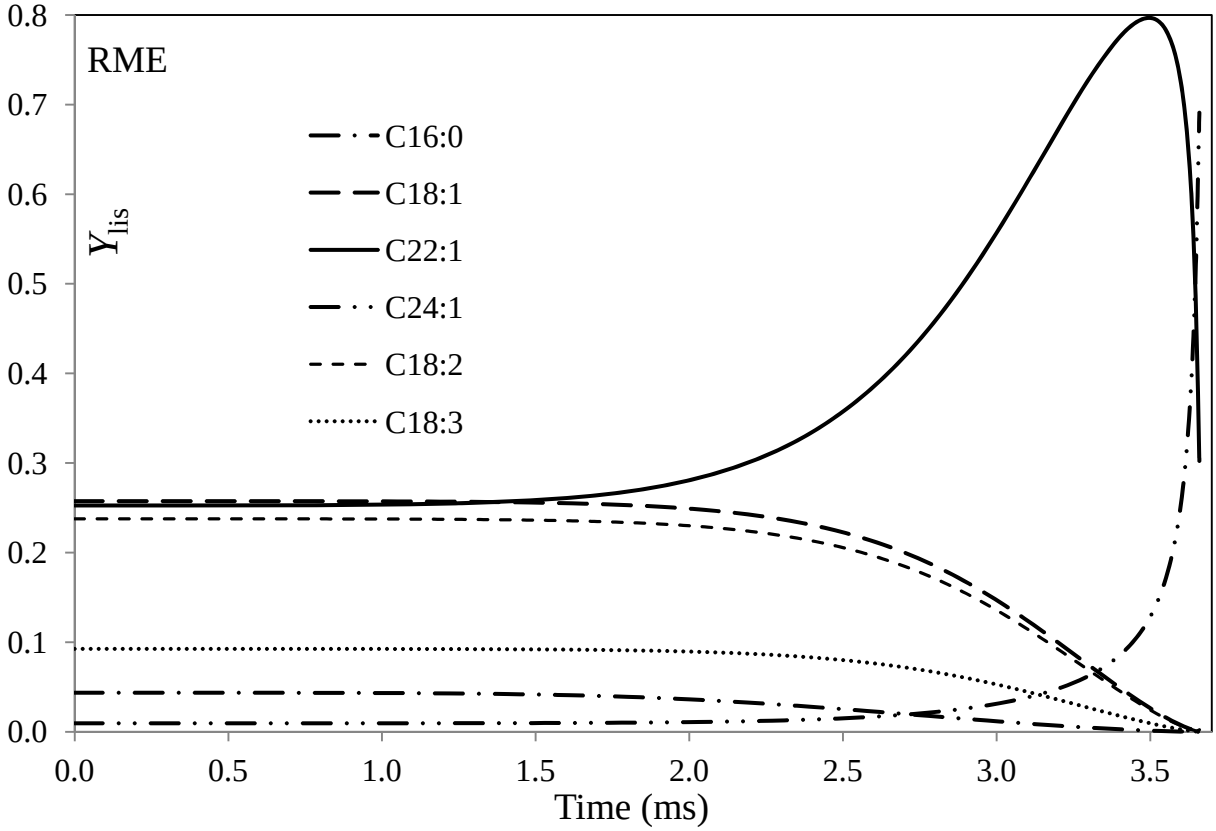
RME
Y_{lis}
C16:0
C18:1
C22:1
C24:1
C18:2
C18:3
0.8
0.7
0.6
0.5
0.4
0.3
0.2
0.1
0.0
0.0
0.5
1.0
1.5
2.0
2.5
3.0
3.5
Time (ms)

Fig. 10

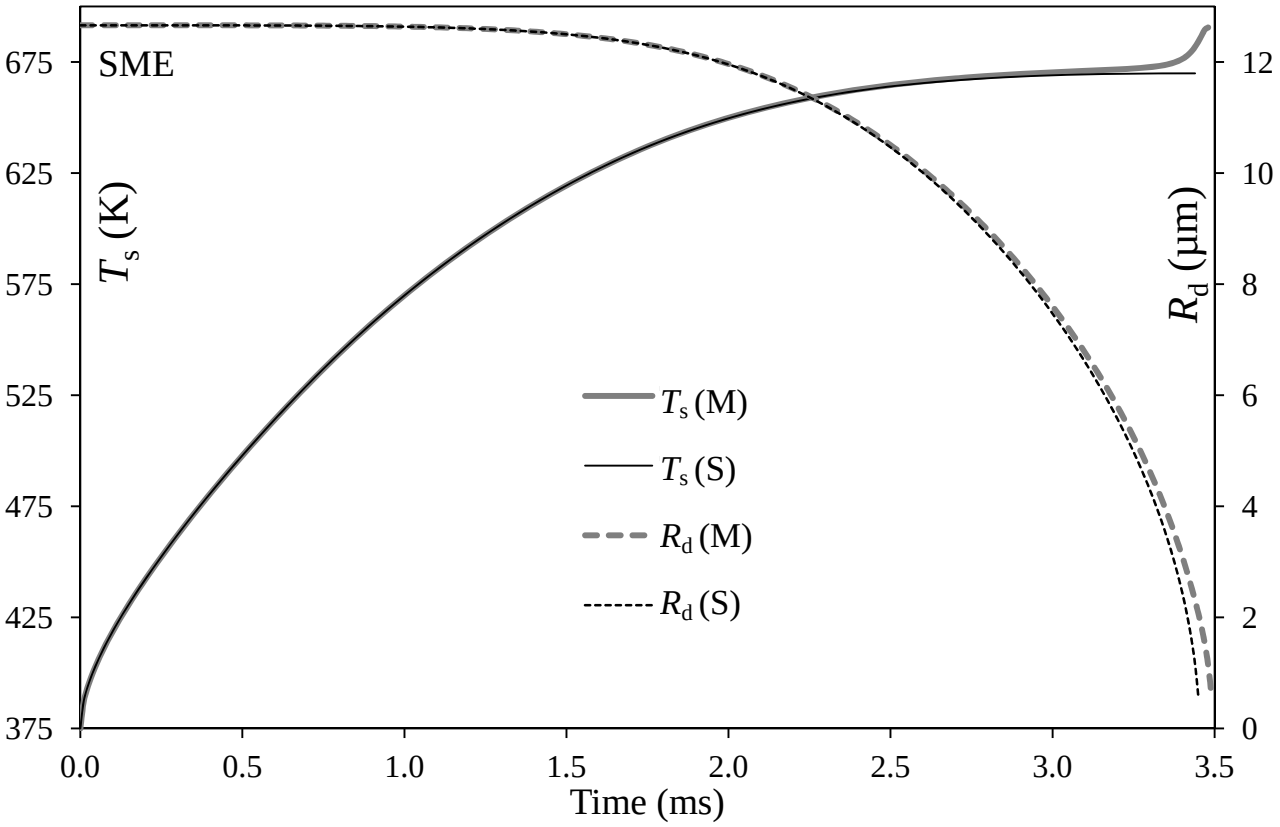
SME
T_s (K)
R_d (μm)
T_s (M)
T_s (S)
R_d (M)
R_d (S)
675
625
575
525
475
425
375
12
10
8
6
4
2
0
0.0
0.5
1.0
1.5
2.0
2.5
3.0
3.5
Time (ms)

Fig. 11

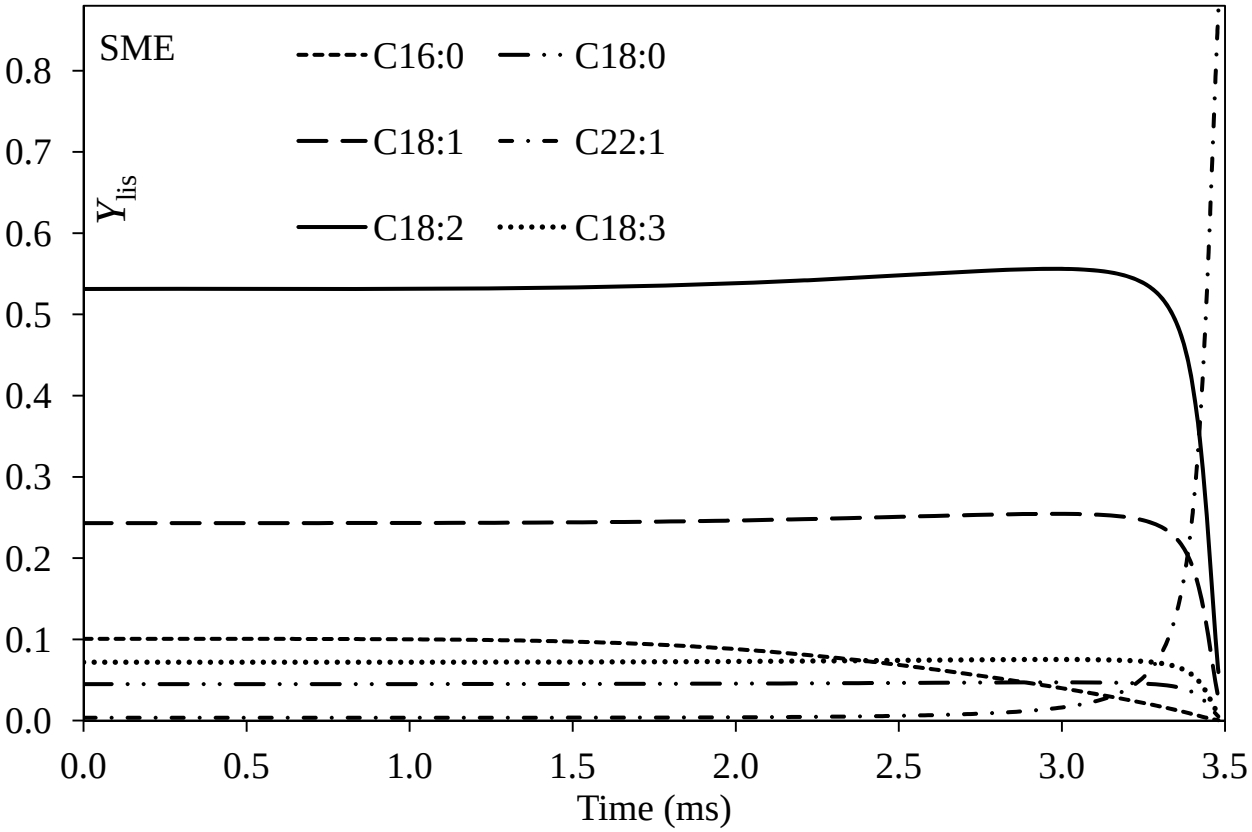
SME
C16:0
C18:0
C18:1
C22:1
C18:2
C18:3
Y_{lis}
0.8
0.7
0.6
0.5
0.4
0.3
0.2
0.1
0.0
0.0
0.5
1.0
1.5
2.0
2.5
3.0
3.5
Time (ms)

Fig. 12

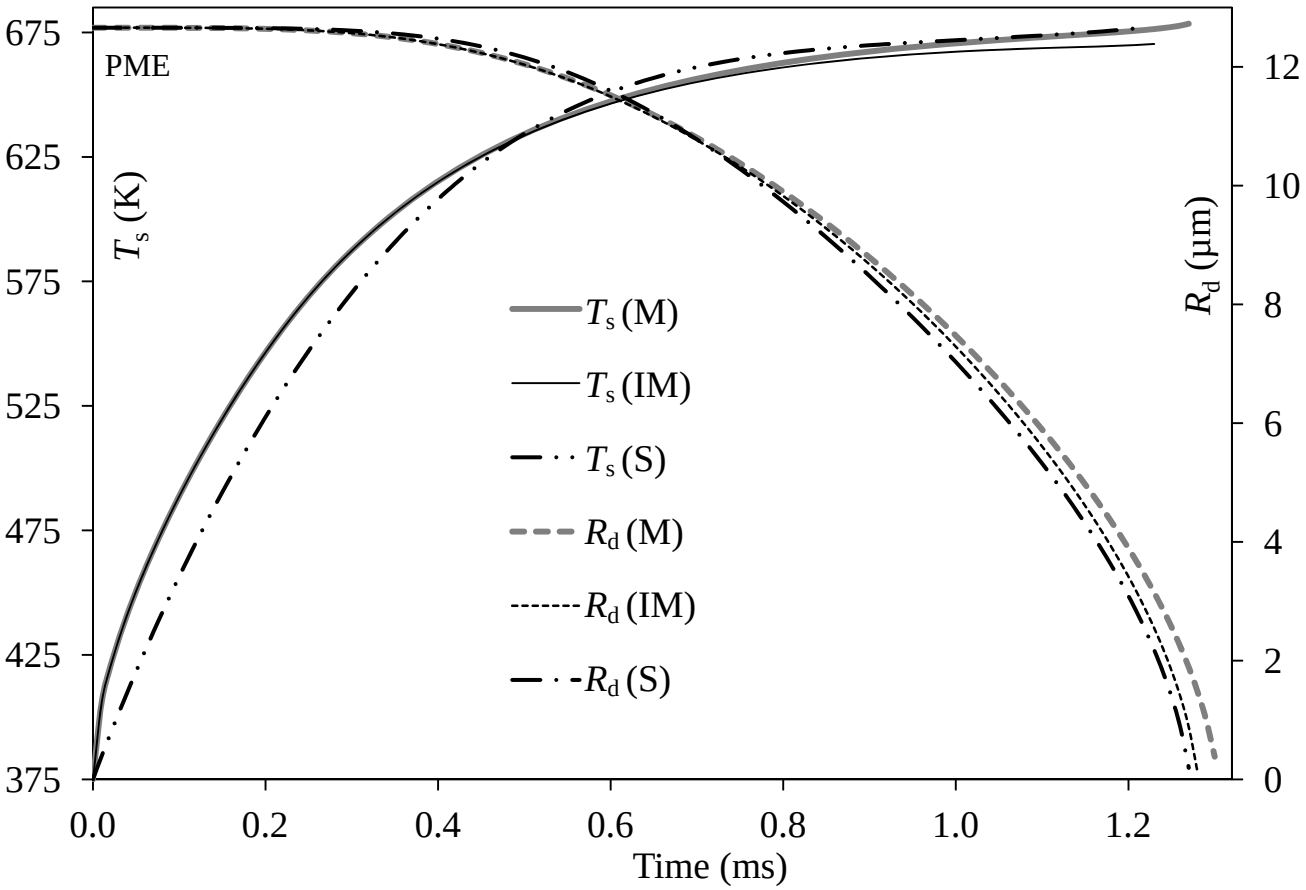
PME
T_s (K)
R_d (μm)
T_s (M)
T_s (IM)
T_s (S)
R_d (M)
R_d (IM)
R_d (S)
675
625
575
525
475
425
375
12
10
8
6
4
2
0
0.0
0.2
0.4
0.6
0.8
1.0
1.2
Time (ms)

Fig. 13

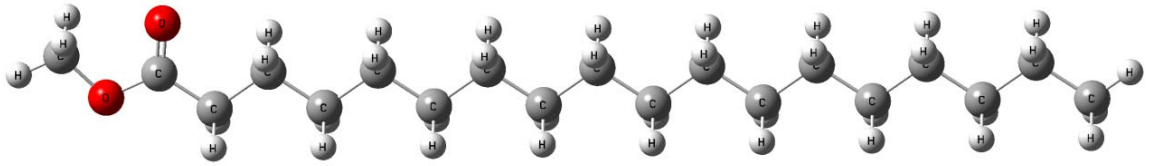

C18:0

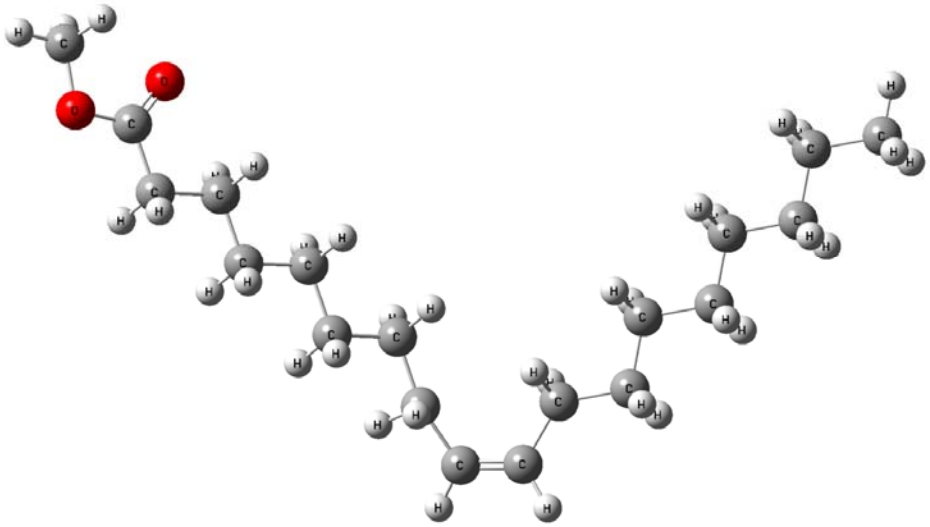

C18:1

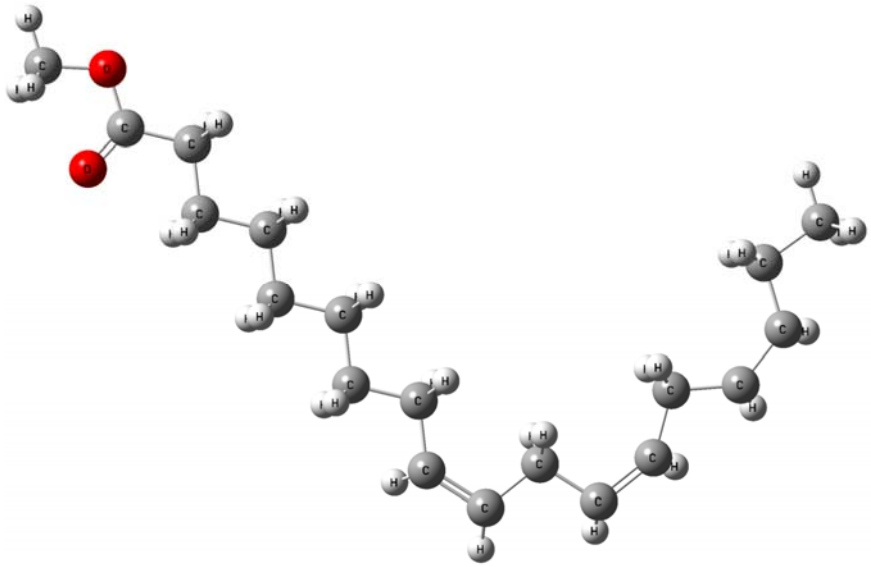

C18:2

Fig. A1